Active galactic nucleus jet feedback in hydrostatic haloes

Rainer Weinberger [1]⋆ Kung-Yi Su,[2] Kristian Ehlert [3,4] Christoph Pfrommer [3] Lars Hernquist,[5] Greg L. Bryan [6,7] Volker Springel [8] Yuan Li [9] Blakesley Burkhart,[7,10] Ena Choi[11,12] and Claude-André Faucher-Giguère [13]

[1]*Canadian Institute for Theoretical Astrophysics, 60 St George Street, Toronto, ON M5S 3H8, Canada*
[2]*Black Hole Initiative, Harvard University, 20 Garden Street, Cambridge, MA 02138, USA*
[3]*Leibniz Institute for Astrophysics, An der Sternwarte 16, D-14482 Potsdam, Germany*
[4]*Institut für Physik und Astronomie, Universität Potsdam, Karl-Liebknecht-Str 24/25, D-14476 Golm, Germany*
[5]*Center for Astrophysics | Harvard & Smithsonian, 60 Garden Street, Cambridge, MA 02138, USA*
[6]*Department of Astronomy, Columbia University, 550 West 120th Street, New York, NY 10027, USA*
[7]*Center for Computational Astrophysics, Flatiron Institute, 162 Fifth Avenue, New York, NY 10010, USA*
[8]*Max Planck Institute for Astrophysics, Karl-Schwarzschild-Str 1, D-85741 Garching, Germany*
[9]*Department of Physics, University of North Texas, 1155 Union Circle 311277, Denton, TX 76203-5017, USA*
[10]*Department of Physics and Astronomy, Rutgers University, 136 Frelinghuysen Road, Piscataway, NJ 08854, USA*
[11]*Department of Physics, University of Seoul, 163 Seoulsiripdaero, Dongdaemun-gu, Seoul 02504, Republic of Korea*
[12]*Korea Institute for Advanced Study (KIAS), 85 Hoegiro, Dongdaemun-gu, Seoul 02455, Republic of Korea*
[13]*Department of Physics and Astronomy and CIERA, Northwestern University, 2145 Sheridan Road, Evanston, IL 60208, USA*

ABSTRACT

Feedback driven by jets from active galactic nuclei is believed to be responsible for reducing cooling flows in cool-core galaxy clusters. We use simulations to model feedback from hydrodynamic jets in isolated haloes. While the jet propagation converges only after the diameter of the jet is well resolved, reliable predictions about the effects these jets have on the cooling time distribution function only require resolutions sufficient to keep the jet-inflated cavities stable. Comparing different model variations, as well as an independent jet model using a different hydrodynamics code, we show that the dominant uncertainties are the choices of jet properties within a given model. Independent of implementation, we find that light, thermal jets with low momentum flux tend to delay the onset of a cooling flow more efficiently on a 50 Myr time-scale than heavy, kinetic jets. The delay of the cooling flow originates from a displacement and boost in entropy of the central gas. If the jet kinetic luminosity depends on accretion rate, collimated, light, hydrodynamic jets are able to reduce cooling flows in haloes, without a need for jet precession or wide opening angles. Comparing the jet feedback with a 'kinetic wind' implementation shows that equal amounts of star formation rate reduction can be achieved by different interactions with the halo gas: the jet has a larger effect on the hot halo gas while leaving the denser, star-forming phase in place, while the wind acts more locally on the star-forming phase, which manifests itself in different time-variability properties.

Key words: galaxies: jets – galaxies: clusters: intracluster medium – galaxies: clusters: general – methods: numerical – hydrodynamics.

1 INTRODUCTION

Feedback from active galactic nuclei (AGNs) has proven to be essential in theoretical studies of galaxy formation. It can be used as a mechanism to break the self-similarity of the stellar mass function (Bower et al. 2006) and bring galaxy colours and the galaxy luminosity function at the massive end in agreement with observations (Croton et al. 2006). State-of-the-art cosmological simulations of galaxy formation rely on these feedback effects to reproduce the observed low rates of star formation in massive central galaxies (Genel et al. 2014; Vogelsberger et al. 2014a, b; Somerville & Davé 2015; Naab & Ostriker 2017) as well as the

neutral gas content in the intergalactic medium (Tillman et al. 2022). The implementations of these feedback effects operate at the resolution limit of these simulations, on 100 pc to kpc scales. AGN-driven winds and jets, however, originate from spatial scales orders of magnitude smaller. Even the most recent simulations designed for high dynamic range are not yet able to fully cover all scales from the central engine to energy deposition (Chatterjee et al. 2019; Lalakos et al. 2022). This unclear outflow behaviour at kpc scales, combined with numerical uncertainties that increase close to the resolution scale, is a key factor currently limiting the predictive power of cosmological galaxy formation simulations.

Observationally, the most direct window into the process of AGN feedback can be found in massive cool-core galaxy clusters (Fabian 2012; McNamara & Nulsen 2012). These clusters show remarkably

⋆ E-mail: rainer@cita.utoronto.ca

low levels of star formation despite high observed X-ray luminosities, indicative of radiative cooling, which has to be balanced by a heating source for the hot gas in these systems to avoid overcooling and substantial star formation. The jet-inflated X-ray dark cavities, ubiquitous in these systems, are the primary candidate for providing this heating (Churazov et al. 2002; Reynolds, Heinz & Begelman 2002). Using the approximate hydrostatic nature of the intracluster medium (ICM), it is possible to infer a heating rate from the sizes and locations of these cavities. The inferred energy injection rate correlates remarkably well with the cooling luminosity of clusters and groups (Bîrzan et al. 2004), indicating that, energetically, jets are able to mediate cooling flows in galaxy groups and clusters and explain their low star formation rates. Yet, the precise mechanism determining how this energy is spatially distributed and how gas is heated is still under debate.

Proposed mechanisms include mixing of the jet lobe material (Hillel & Soker 2017), convective energy transport (Yang & Reynolds 2016b; Chen, Heinz & Enßlin 2019), turbulent dissipation (Fujita, Cen & Zhuravleva 2020), shock heating (Li, Ruszkowski & Bryan 2017), sound and gravity waves (Reynolds, Balbus & Schekochihin 2015; Bambic & Reynolds 2019), cosmic ray protons (Guo & Oh 2008; Jacob & Pfrommer 2017a, b; Ruszkowski, Yang & Reynolds 2017), thermal conduction (Yang & Reynolds 2016a; Kannan et al. 2017; Barnes et al. 2019), and a combination of a number of the above-mentioned effects (e.g. Soker 2019; Su et al. 2020).

One of the underlying problems at the heart of studying how AGN jet energy is distributed is the enormous dynamic range of scales involved. This implies that either simulations cover the long-term evolution, modelling the system for several cooling times to ensure that star formation is affected and a steady state in the cooling flow is reached (e.g. Dubois et al. 2010; Gaspari et al. 2011; Gaspari, Brighenti & Temi 2012; Prasad, Sharma & Babul 2015; Meece, Voit & O'Shea 2017; Beckmann et al. 2019; Martizzi et al. 2019; Huško et al. 2022), or simulations resolve jets and their propagation in more detail, but are limited to one to two orders of magnitude shorter simulation times. The latter simulations cover only a buoyancy time-scale or even only the jet propagation phase (e.g. Bourne, Sijacki & Puchwein 2019; Duan & Guo 2020; Bourne & Sijacki 2021; Komissarov & Porth 2021; Talbot, Bourne & Sijacki 2021; Huško & Lacey 2022; Massaglia et al. 2022; Perucho, Martí & Quilis 2022; Talbot, Sijacki & Bourne 2022). Our work is at the intersection of these two approaches, trying to link high-fidelity jet propagation studies with studies of self-regulated cooling flows in hydrostatic haloes in an overall attempt to create a predictive AGN jet feedback model. In particular, we investigate whether resolved hydrodynamic jets are able to moderate cooling flows in galaxy clusters over Gyr time-scales and how this ability depends on numerical resolution, model choices, and implementation/code details.

The paper is structured as follows: We present the simulation methods and set-up in Section 2 and study the jet propagation of a single outburst in Section 3 and its effect on hydrostatic haloes in Section 4. In Section 5, we present self-regulated simulations and discuss the impact of AGN jets on them. Finally, we present our conclusions from this study in Section 6.

2 MODEL AND SIMULATION SET-UP

To get a sense of how AGN jets act in an ICM environment, we model an isolated hydrostatic halo of mass 10^{14} M$_\odot$ at $z = 1$, using an analytical gravitational potential, and perform simulations including radiative cooling, star formation, and AGN feedback. In a first set of simulations, we inject AGN feedback at fixed luminosity

$\dot{E} = 10^{45}$ erg s^{-1} using two independent jet model implementations and different simulation codes, AREPO (Springel 2010) and GIZMO (Hopkins 2015), as well as an AGN wind model. These simulations only cover the onset of a cooling flow, and do not end up forming any stars in their 250 Myr simulation time. A second set of simulations uses the same initial conditions, but now the black hole accretion rate is estimated using the Bondi rate and 10 per cent of the accreted rest-mass energy is used as feedback energy. These runs are evolved for several central cooling times (in total 2 Gyr), to ensure that self-regulation actually sets in and to be able to study the effects on the star formation rate.

2.1 Initial conditions

Unlike a number of similar studies that focus on matching their model to local galaxy clusters, we choose to base our initial conditions on cosmological simulations of galaxy clusters at redshift $z = 1$. This is done for a number of reasons: first, starting with a local cluster implies simulating into the future, and secondly, the ICM conditions can change with redshift. Concretely, high-redshift galaxy clusters are more frequently found to be in a cool-core state (McDonald et al. 2013, 2017; Barnes et al. 2019) with higher cooling luminosities and AGN powers (Weinberger et al. 2018), making the cooling flows more prominent. Considering that our assumption of an isolated hydrostatic halo degrades with increasing redshift, we choose redshift $z = 1$ as a compromise. Note that the simulation itself neglects cosmological expansion and all length-scales are stated in proper coordinates.

The hydrostatic halo in this study is a fit to $z = 1$ haloes in the IllustrisTNG cosmological simulations (Marinacci et al. 2018; Naiman et al. 2018; Nelson et al. 2018; Pillepich et al. 2018b; Springel et al. 2018). We use a truncated NFW profile (Navarro, Frenk & White 1996) and singular isothermal sphere profile to fit the enclosed gravitating mass:

$$M_{\rm enc}(r) = \min\left\{4\pi\rho_{\rm NFW}R_{\rm s}^3\left[\ln\left(\frac{r+R_{\rm s}}{R_{\rm s}}\right) - \frac{r}{r+R_{\rm s}}\right], M_{\rm NFW}\right\}$$
$$+ \min\left\{\frac{r\,M_{\rm ISO}}{R_{\rm ISO}}, M_{\rm ISO}\right\}, \tag{1}$$

where

$$\rho_{\rm NFW} = M_{\rm NFW}\left[4\pi\,R_{\rm s}^3\,\left(\ln(1+c_{\rm NFW}) - \frac{c_{\rm NFW}}{1+c_{\rm NFW}}\right)\right]^{-1}, \tag{2}$$

$$R_{\rm s} = R_{\rm NFW}\,c_{\rm NFW}^{-1}. \tag{3}$$

Note that we fixed $R_{\rm ISO} = 0.1$ Mpc to avoid degeneracies in the fit.

The gas density profile is fitted with a double beta profile:

$$\rho(r) = \left(\frac{\rho_1}{1+(r/r_1)^2}\right)^{3/2\,\beta_1} + \left(\frac{\rho_2}{1+(r/r_2)^2}\right)^{3/2\,\beta_2}. \tag{4}$$

The thermal pressure is adjusted such that the gas halo is initially in hydrostatic equilibrium. To break the exact spherical symmetry, the gas velocities in the central region ($r < 600$ kpc) follow a Kolmogorov power spectrum, normalized to a root mean square velocity of 75 km s^{-1}.[1] Gas further out is initially at rest. We place a black hole at rest in the centre of the potential, and keep it fixed at this position during the simulation. All the parameters related to the initial conditions are shown in Table 1 and the profiles of density, temperature, and

---

[1]This is lower than the measured velocity dispersion in local massive galaxy clusters (Zhuravleva et al. 2014; Hitomi Collaboration 2016; Li et al. 2020).

Table 1. Parameters for the initial conditions. The last three rows specify the turbulent power spectrum of the initial gas velocities. The resulting cooling luminosity of the halo gas is approximately 10^{44} erg s^{-1}.

Parameter	Value
M_{NFW}	10^{14} M$_\odot$
R_{NFW}	1.0 Mpc
c_{NFW}	2.84
M_{ISO}	3.7×10^9 M$_\odot$
R_{ISO}	0.1 Mpc
ρ_1	1.13×10^{-25} g cm^{-3}
r_1	26.3 kpc
β_1	1.89
ρ_2	7.16×10^{-27} g cm^{-3}
r_2	303 kpc
β_2	1.42
σ_{gas}	75 km s^{-1}
k_{min}	8.4 Mpc^{-1}
k_{max}	16.8 Mpc^{-1}
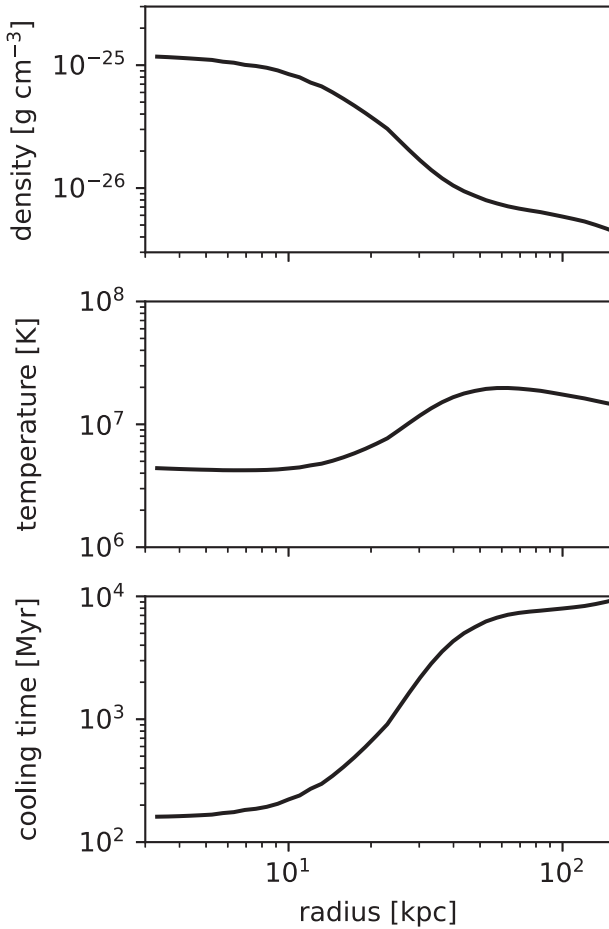
Figure 1. Density, temperature, and cooling time profiles of initial conditions.

cooling time ($t_c = -\varepsilon_{\text{th}} \dot{\varepsilon}_c^{-1}$, where ε_{th} is the thermal energy density and $\dot{\varepsilon}_c^{-1}$ is its rate of change due to radiative cooling) are indicated in Fig. 1.

The discretization of the hydrodynamic quantities follows the approach of Pakmor et al. (2011) and Ohlmann et al. (2016) and ensures that both volume-discretized schemes such as AREPO and

mass-discretized schemes such as employed in the meshless finite mass scheme used in GIZMO can handle the same input. We employ a radius-dependent mass per resolution element i following

$$m_i = m_0 \exp\left(\frac{r}{r_0}\right), \tag{5}$$

with $m_0 = 9.4 \times 10^4$ M$_\odot$ and $r_0 = 3 \times 10^2$ kpc, but limiting the volume of a resolution element (defined as its mass divided by its density) to a maximum of 5×10^7 kpc^3. The latter is only there to avoid numerical problems in the outskirts and has no impact on the regions studied in this work. The overall simulation domain has the side length 6×10^3 kpc, which ensures that the region of interest is free of boundary effects. During the simulation, cells are refined and derefined to stay within a factor of 2 of the target mass m or the respective volume constraint if it applies. As an additional criterion, cells that have neighbouring cells with a volume less than 0.1 of their own volume are refined to avoid strong resolution gradients that would degrade the accuracy of the simulation. We verified that all presented results are unchanged when using $m_0 = 7.5 \times 10^5$ M$_\odot$, implying that the results do not depend on the resolution of the background.

We note that in the following 'resolution' refers to an additional resolution parameter for the jet material, which has proven to be necessary in these kinds of studies (Bourne & Sijacki 2017), in particular for low-density jets. This criterion differs for the different models and is not present for the IllustrisTNG kinetic feedback.

2.2 Equations and models

We solve the equations of ideal hydrodynamics under the influence of a static external gravitational potential; additionally, radiative cooling from primordial elements and metal lines is included, assuming a constant metallicity of 0.3 times the solar value. To balance the cooling flow, we use three different feedback injection methods for AGN feedback and assess the uncertainties in modelling and its consequences for galaxy cluster modelling: first, the jet model presented in Weinberger et al. (2017b) with some modifications as discussed in the next subsection; secondly, the jet model recently introduced by Su et al. (2021); and thirdly, the kinetic AGN wind model used in the IllustrisTNG cosmological simulations (Weinberger et al. 2017a). While most of the simulations are run with the finite-volume moving mesh code AREPO (Springel 2010), the runs employing the Su et al. (2021) model are using the meshless finite mass technique in GIZMO (Hopkins 2015), thus enabling us to study the effects of differences in hydrodynamics solver (and radiative cooling implementation).

The simulations performed with AREPO rely on the metal cooling and star formation modelling described in Vogelsberger et al. (2013) with updated parameters from Pillepich et al. (2018a), consistent with the IllustrisTNG simulations. The simulations performed with GIZMO are using the Hopkins et al. (2018) model, consistent with the FIRE-2 model.

2.2.1 RW jet model

For the self-regulated simulations in this work, the algorithm for the jet injection needs to be adjusted from its original implementation in Weinberger et al. (2017b). Originally, the basic idea was to set up a 'small-scale jet' evolved up to the resolution limit with a clear, separated jet region with density ρ_{jet}, and the remaining mass distributed into a surrounding 'buffer region', taking into account adiabatic compression terms, ensuring exact gas mass conservation
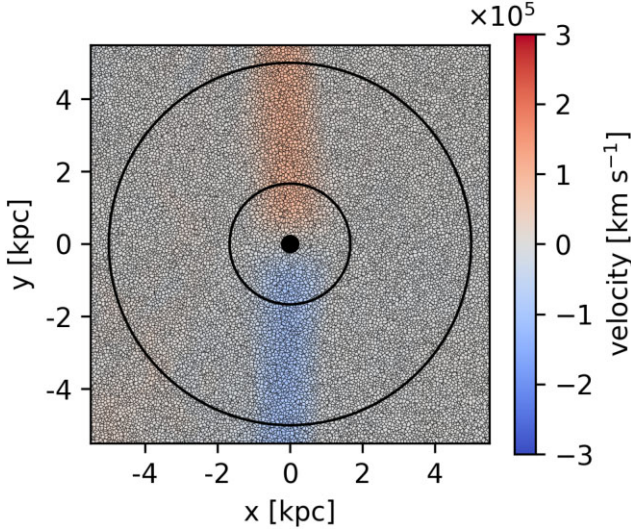
Figure 2. Schematic of the black hole surroundings, including jet (central sphere) and accretion estimate (outer spherical shell) regions. The colour scale indicates the velocity of cells in the jet propagation direction. The schematic shows the highest resolution, *rw jet a 5* simulation in which all regions are well sampled.

in the system, and adding the remaining energy as kinetic energy in the jet. This approach works well for non-radiative hydrodynamics, but adding mass into an arbitrarily sized buffer region in simulations including radiative cooling leads to spurious effects. This led to a redesign of aspects of the algorithm to better fit the needs of self-regulated and ultimately cosmological simulations.

Around the black hole, a radius is defined such that the kernel-weighted number of gas cells in this region reaches a pre-defined value (this is identical to the procedure used e.g. in Weinberger et al. 2017a). Unlike in previous work, this sphere is then separated into an inner sphere with one-third of this radius ($r \leq 1.65$ kpc) and an outer spherical shell (1.65 kpc $< r < 5$ kpc). The inner sphere is used to set up the jet and the outer spherical shell to estimate the surrounding properties, i.e. to calculate the ambient pressure and properties used in the accretion rate estimate. Fig. 2 shows the mesh and velocity field around the black hole and the locations of the jet injection region (inner sphere) and outer spherical shell are indicated by circles.

In the inner sphere, we set up gas with density $\rho_{\rm jet} = 10^{-28}$ g cm^{-3} (model *a*), $\rho_{\rm jet} = 10^{-27}$ g cm^{-3} (model *b*), $\rho_{\rm jet} = 10^{-26}$ g cm^{-3} (model *c*), and $\rho_{\rm jet} = 10^{-25}$ g cm^{-3} (model *d*). Given the central density of the initial conditions of $<\rho> \approx 10^{-25}$ g cm^{-3}, the density contrast $\eta = \rho_{\rm jet} \langle \rho \rangle^{-1}$ ranges from 10^{-3} to unity. In the following, we will refer to jets with low η as light or low-density and jets approaching $\eta = 1$ as dense or heavy. Mass is removed from (or sometimes, though more rarely, added to) the region to achieve this. This net removal of mass Δm is logged and used in the accretion routine if needed, and ΔE, the thermal energy corresponding to a specific energy $<u>$ of the surrounding gas, is removed from the system, i.e.

$$\Delta m = \sum_i (\rho_i - \rho_{\rm jet}) V_i, \tag{6}$$

$$\Delta E_{\rm mass} = \Delta m \langle u \rangle, \tag{7}$$

where the sum is over all cells i in the inner sphere, V_i denotes the volume of cell i, and $<u>$ is a kernel-averaged estimate of the specific thermal energy of the outer spherical shell.

The specific internal energy of the gas in the inner sphere (i.e. the jet region) $u_{\rm jet,\,i}$ is increased for the gas to be in equilibrium with the

pressure in the outer spherical shell $<p>$. To ensure no violation of the second law of thermodynamics, and to avoid numerical instabilities, we only allow for increases in specific thermal energy as well as in thermal energy on a per cell basis; i.e. cells that are already overpressured are kept this way:

$$u_{\rm jet,i} = \max \left(u_i, \langle p \rangle \left((\gamma - 1) \rho_{\rm jet} \right)^{-1} \right), \tag{8}$$

where γ denotes the adiabatic index of the fluid. The energy required to establish pressure equilibrium

$$\Delta E_{\rm therm,i} = \rho_{\rm jet} V_i \left(u_{\rm jet,i} - u_i \right) \tag{9}$$

is subtracted from the available energy $E_{\rm tot}$ and the remaining energy (the dominant part) is used for momentum kicks in bipolar directions,

$$E_{\rm jet,\,kin} = E_{\rm tot} - \sum_i \Delta E_{\rm mass,i} - \sum_i \Delta E_{\rm therm,i}. \tag{10}$$

Note that the momentum is directed in strictly bipolar directions without an opening angle, with the exception of *rw wind*, for which a $60°$ opening angle (i.e. velocity kick direction up to $60°$ off the jet axis) is applied. The typical velocities at the injection scale can be estimated by

$$\dot{E} \sim \frac{1}{2} \rho_{\rm jet} v_{\rm jet}^3 A, \tag{11}$$

where $\dot{E} = 10^{45}$ erg s^{-1} is the jet kinetic luminosity and $A = (1.65$ kpc$)^2 \pi = 8.6$ kpc^2 is the cross-section of the injection region. The typical velocities are thus 6×10^4 km s^{-1} (0.2 times the speed of light) for model *a* ($\rho_{\rm jet} = 10^{-28}$ g cm^{-3}) to 6×10^3 km s^{-1} (0.02 times the speed of light) for model *d* ($\rho_{\rm jet} = 10^{-25}$ g cm^{-3}). As shown in Fig. 2, the achieved velocities can be slightly higher due to a weighted injection of kinetic energy that awards on jet-axis cells a larger than average velocity kick and avoids shear discontinuities at injection.

The kinetic luminosity is chosen to match the cooling losses over the simulation time. This approach is motivated by the cumulative energy measured by X-ray cavities roughly balancing cooling losses (e.g. Bîrzan et al. 2004; Olivares et al. 2022). Comparing to radio properties of jets (see e.g. Hardcastle & Croston 2020, for a review), this kinetic luminosity lies about an order of magnitude above the Fanaroff & Riley (1974) type I/II divide in the Kaiser & Alexander (1997) model. However, since the jet is propagating in a galaxy cluster, we none the less expect the resulting morphology to be substantially affected by its dense environment (Owen & Ledlow 1997; Mingo et al. 2019). We would thus expect the resulting radio jets to represent the luminous end of the FRI population in dense environments, which are mildly relativistic on kpc scales and decelerate smoothly with substantial entrainment from surrounding gas (Bicknell 1994; Laing & Bridle 2014) and reach trans-sonic velocities on or slightly beyond kpc scales (Bicknell 1995).

Note that while some of the jets in our simulations are reaching mildly relativistic speeds, we solve the equations of non-relativistic hydrodynamics in our simulations since we mostly focus on the long-term evolution of the system. The precise morphology and properties of the active jet, however, could be affected by these omitted effects (English, Hardcastle & Krause 2016; Perucho, Martí & Quilis 2019; Yates-Jones et al. 2022). For the long-term evolution, however, the ratio of energy to momentum flux carried is crucial, which in the non-relativistic case is proportional to the velocity. All the jets are internally supersonic on kpc scales, with Mach numbers between 1.5 and 4, as detailed in Table 2 (see e.g. Hardcastle & Krause 2014; Guo 2016, on the impact of internal Mach number on lobe properties), which is, for the high-resolution runs, slightly higher

Table 2. List of simulations and their parameter variations. From left to right, we show the name, the model (rw17 refers to Weinberger et al. 2017b, rw 17a to Weinberger et al. 2017a, and su21 to Su et al. 2021), the simulated time, the jet density ρ_{jet}, which is an input parameter, the approximate relative density ratio relative to the central density in the initial conditions η and the measured jet Mach number $\mathcal{M}$ on kpc scales after 6.25 Myr, and finally the mass resolution in the jet region. All single outburst calculations have a jet kinetic luminosity $\dot{E} = 10^{45}$ erg s^{-1} for a time of 25 Myr. The simulations starting with kys are performed with the GIZMO code, while all other runs are performed with AREPO.

Single outburst Name	Model	Time	Jet density ρ_{jet}	Relative density η	Jet Mach number $\mathcal{M}$	Resolution
rw jet a 1	rw17	250 Myr	10^{-28} g cm^{-3}	10^{-3}	1.5	2.5×10^3 M$_\odot$
rw jet a 2	rw17	250 Myr	10^{-28} g cm^{-3}	10^{-3}	2.0	3.1×10^2 M$_\odot$
rw jet a 3	rw17	250 Myr	10^{-28} g cm^{-3}	10^{-3}	2.5	39 M$_\odot$
rw jet a 4	rw17	250 Myr	10^{-28} g cm^{-3}	10^{-3}	3.0	4.9 M$_\odot$
rw jet a 5	rw17	25 Myr	10^{-28} g cm^{-3}	10^{-3}	3.0	0.61 M$_\odot$
rw jet b 2	rw17	250 Myr	10^{-27} g cm^{-3}	10^{-2}	2.5	9.4×10^3 M$_\odot$
rw jet c 2	rw17	250 Myr	10^{-26} g cm^{-3}	10^{-1}	3.0	9.4×10^4 M$_\odot$
rw jet d 2	rw17	250 Myr	10^{-25} g cm^{-3}	1	4.0	3.1×10^5 M$_\odot$
rw wind d 2	rw17	250 Myr	10^{-25} g cm^{-3}	1	4.0	3.1×10^5 M$_\odot$
tng	rw17a	250 Myr	Ambient	1	–	9.4×10^4 M$_\odot$
rw no jet	–	250 Myr	–	–	–	9.4×10^4 M$_\odot$
kys jet b	su21	250 Myr	10^{-27} g cm^{-3}	10^{-2}	3.0	4.5×10^2 M$_\odot$
kys jet c	su21	250 Myr	10^{-26} g cm^{-3}	10^{-1}	4.5	4.5×10^3 M$_\odot$
kys no jet	–	250 Myr	–	–	–	9.4×10^4 M$_\odot$
Self-regulated						
jet	rw17	2000 Myr	10^{-28} g cm^{-3}	10^{-3}	Variable	3.1×10^2 M$_\odot$
tng	rw17a	2000 Myr	Ambient	1	–	9.4×10^4 M$_\odot$
no AGN	–	2000 Myr	–	–	–	9.4×10^4 M$_\odot$

Table 3. Model and wind parameters of the TNG kinetic wind model. The model parameters are defined in equations (18)–(20); the wind velocity v_{wind}, density ρ_{wind}, and mass flux $\dot{m}_{wind}$ are derived using a single injection event and deriving characteristic quantities (using the typical injection sphere radius of $h = 1$ kpc).

Model parameters	
n_{ngb}	64
f_{re}	20
σ_{DM}	3.3×10^2 km s^{-1}
$\epsilon_{f, kin}$	0.1
Wind properties (derived)	
v_{wind}	1.5×10^3
ρ_{wind}	10^{-25} g cm^{-3}
$\dot{m}_{wind}$	7 M$_\odot$ yr^{-1}

than the intended trans-sonic regime and a consequence of avoiding relativistic specific internal energies. We leave exploration of these effects to future work.

The accretion rate is estimated from the outer spherical shell, with the properties such as density and sound speed estimated in a kernel-weighted fashion. From these quantities, the accretion rate $\dot{m}_{acc}$ is then calculated using the Bondi accretion rate,

$$\dot{m}_{acc} = 4\pi G^2 m_{BH}^2 \langle \rho \rangle \langle c_s \rangle^{-3} \quad (12)$$

where G is the gravitational constant, m_{BH} is the black hole mass, and $<\rho>$ and $\langle c_s \rangle$ are kernel-averaged surrounding density and sound speed, respectively. While the precise functional form of accretion might in practice differ substantially from the employed Bondi formula (Gaspari, Temi & Brighenti 2017), studies with similar set-ups have found no strong dependence of the self-regulation on the accretion formula as long as it triggers rapid accretion in the presence of cold, dense gas (Meece et al. 2017; Ehlert et al. 2023).

We note that for the first set of runs we keep the radius of the jet injection routine constant (1.65 kpc for the jet region) instead of estimating it from the number of surrounding gas cells. This is done to produce resolution studies that are easier to interpret, in which all effects are attributable to the hydrodynamic resolution of the jet, instead of resolution effects due to the feedback model. We also performed these simulations with a fixed number of cells in the black hole surroundings and hence a resolution-dependent physical radius of the injection region of the jet (not shown here) and found no qualitative differences.

Cells that include gas originating from the jet with a mass fraction exceeding 10^{-3} are additionally refined to a target volume V_{target}; thus, the mass for these cells is

$$m_i = \rho_i V_{target}, \quad (13)$$

again refined and derefined accordingly if the actual mass differs by more than a factor of 2. Note that we define the resolution in Table 2 as $\rho_{jet} V_{target}$ to be able to consistently use mass resolution.

2.2.2 KYS jet model

As an independent model comparison, we use the jet launching technique presented in Su et al. (2021), utilizing a particle spawning method (see also Torrey et al. 2020 and Wellons et al. 2022). This method is implemented into the GIZMO code, which solves the Euler equations using a meshless finite mass scheme. A jet is launched from the centre by creating new mass elements at a pre-defined mass flux and attributing a mass, velocity v_{jet}, and temperature T to each resolution element. To match this model to the previous one, we calculate the temperature using ρ_{jet} and external pressure in the initial conditions and the velocity v_{jet} using

$$\dot{E} = \frac{1}{2}\rho_{jet} v_{jet}^3 A + u_{jet}\rho_{jet} v_{jet} A. \quad (14)$$

To get the mass flux $\dot{M}$, we use

$$\dot{M} = \rho_{\text{jet}} v_{\text{jet}} A. \tag{15}$$

For the model comparison, we use two different jet parameters

$\rho_{\text{jet}} = 10^{-27} \text{ g cm}^{-3}; \dot{E} = 10^{45} \text{ erg s}^{-1}$ matched to

$v_{\text{jet}} = 2.6 \times 10^4 \text{ km s}^{-1}; \dot{M} = 3.5 \, \text{M}_\odot \text{ yr}^{-1}; T = 4.8 \times 10^9 \text{ K}, \tag{16}$

for model *b* and

$\rho_{\text{jet}} = 10^{-26} \text{ g cm}^{-3}; \dot{E} = 10^{45} \text{ erg s}^{-1}$ matched to

$v_{\text{jet}} = 1.3 \times 10^4 \text{ km s}^{-1}; \dot{M} = 17 \, \text{M}_\odot \text{ yr}^{-1}; T = 4.8 \times 10^8 \text{ K}, \tag{17}$

for model *c*. The internal Mach number in the jet is between 3 and 4.5 at the injection scale, as detailed in Table 2. The mass of each spawned particle i is $m_i = 4.5 \times 10^2$ and $4.5 \times 10^3 \, \text{M}_\odot$ for the two runs, respectively.[2]

2.2.3 TNG kinetic winds

As a comparison with established models that were previously used in cosmological simulations, we run simulations using the kinetic wind model of Weinberger et al. (2017a) with parameters listed in Table 3. Unlike in the cosmological context, we enforce the model to be always in kinetic wind and never in thermal mode. This is done because the kinetic wind mode has been shown to be the dominant one in quenching of massive galaxies and keeping galaxies quiescent (Weinberger et al. 2018). The kinetic wind mode is thus also responsible for reducing cooling flows.

The injection region for the wind is a sphere around the black hole with radius h

$$n_{\text{ngb}} = \sum_i \frac{4\pi}{3} \frac{h^3 m_i}{m_0} w(r_i), \tag{18}$$

where the number of neighbouring gas cells $n_{\text{ngb}} = 64$ is a free parameter, m_i is the mass of cell i, m_0 is the target gas mass, $w(r_i)$ is an (SPH-like) cubic spline kernel with dimensions of an inverse volume and softening length h, and r_i is the distance of the cell to the black hole. In the case of the fixed kinetic luminosity runs, the available energy ΔE simply accumulates, in the case of the self-regulated simulation,

$$\Delta E = \int \epsilon_{\text{f,kin}} \dot{m}_{\text{acc}} c^2 \mathrm{d}t, \tag{19}$$

where $\epsilon_{\text{f, kin}} = 0.1$, $\dot{m}_{\text{acc}}$ is the accretion rate determined by the Bondi accretion rate formula in equation (12), and c denotes the speed of light. The injection of the wind happens in a pulsed fashion, with a pulse being injected if the accumulated energy ΔE is equal or exceeds

$$E_{\text{inj,min}} = f_{\text{re}} \frac{1}{2} \sigma_{\text{DM}}^2 m_{\text{enc}}, \tag{20}$$

where in this simulation we use a fixed $\sigma_{\text{DM}} = 3.3 \times 10^2 \text{ km s}^{-1}$ since the presented simulations do not contain live dark matter particles to be measured on the fly. m_{enc} is the enclosed gas mass within the injection sphere and $f_{\text{re}} = 20$ is a free parameter controlling the frequency of pulses. Once the available energy ΔE exceeds $E_{\text{inj, min}}$,

a momentum kick

$$\Delta \boldsymbol{p}_i = m_i \sqrt{\frac{2 \, \Delta E \, w(r_i)}{\langle \rho \rangle}} \hat{\boldsymbol{n}} \tag{21}$$

is applied to all cells i within the injection sphere. Note that there is a single injection direction $\hat{\boldsymbol{n}}$ with no opening angle. However, the injection direction is chosen randomly from a unit sphere after each pulse, resulting in a spherical injection on average.

These parameters imply that the small-scale wind of an individual injection event reaches velocities of $1.5 \times 10^3 \text{ km s}^{-1}$. The model uses the ambient density and only adds momentum kicks without injecting mass, making a definition of a mass flux somewhat ambiguous. Using the initial surrounding density of $10^{-25} \text{ g cm}^{-3}$ and the injection region radius of about 1 kpc, this results in a mass flux of 7 $\text{M}_\odot \text{ yr}^{-1}$. In summary, the parameters are close, but not identical to IllustrisTNG.

2.3 Summary of simulations

The main challenge in this study is the dynamic range in time. High spatial resolution in the jet requires very short time-steps, while covering several central cooling times requires an overall simulation time of the order of several Gyr. Even with state-of-the-art computing capabilities and numerical optimizations, this is challenging and would prohibit model variations.

To overcome these difficulties, we use two different types of simulations *starting from the same initial conditions*. First, we run fixed jet power simulations with $\dot{E} = 10^{45} \text{ erg s}^{-1}$, beginning from a single outburst lasting for 25 Myr, i.e. a total energy injection of 8×10^{59} erg and an overall simulation time up to 250 Myr.[3] Note that the cooling luminosity in the halo is approximately $10^{44} \text{ erg s}^{-1}$. These simulations will be analysed in Sections 3 and 4. Secondly, we run a few self-regulated simulations in which the feedback energy is calculated using the accretion rate. These runs are evolved for 2 Gyr and establish an equilibrium between cooling flow and star formation. For the latter simulation, we compare two models, the IllustrisTNG kinetic wind (*tng*) and the *rw jet a 2* model (*jet*). These simulations will be shown in Section 5. A summary of the simulations can be found in Table 2. We restrict the resolution study to model *rw jet a* since this lowest density jet tends to be most sensitive to changes of resolution.

Note that all these simulations use non-relativistic ideal hydro-dynamics for simplicity. Magnetic fields are not included, yet for all three models studies highlighting their effect exist. Weinberger et al. (2017b) showed that while a weak magnetization increases the stability of the lobes, even hydrodynamical lobes of the jets presented in this work are stable over the relevant time-scales. Su et al. (2021) found magnetic field to play a minor role for feedback unless the injected magnetic fluxes are $>10^{44} \text{ erg s}^{-1}$ in a set-up similar to the one presented in this work. Finally, Ehlert et al. (2023) studied self-regulated cool-core systems and found magnetic fields to dominate the dynamics of cold gas, while they connect the cold to the hot ICM phase, thereby enabling efficient (angular) momentum transport from one phase to the other (Wang et al. 2021). This effect seems to be important for shaping the thermodynamics and kinematics of the cold phase on time-scales relevant for long-time self-regulation of the ICM (Ehlert et al. 2023), which goes beyond the focus of this study. Relativistic effects to the equation of state of the jet material or its cooling functions are not included. The jet material is just

---

[2]Note that the mass per jet resolution element in the simulations run with GIZMO is higher than that for the AREPO simulations in order to ensure both are converged.

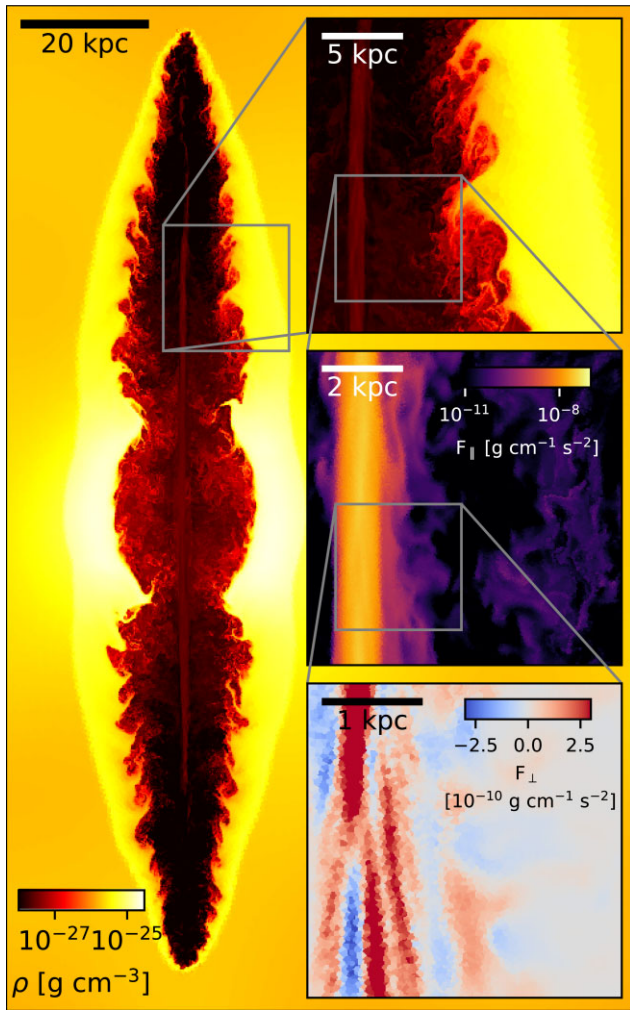[3]The highest resolution jet stops at 25 Myr due to computational limitations.

Figure 3. Density slice (main panel and upper inlay) of *rw jet a 5* after 25 Myr. The central inlay shows the momentum flux density in the jet direction $F_\parallel$, and the bottom panel shows the momentum flux perpendicular to the jet direction $F_\perp$. Its change of sign indicates body modes in the jet flow. The shape of the resulting cavity differs from observed X-ray cavities likely due to the absence of density fluctuations in its propagation direction as well as its constant luminosity.

modelled as very hot, relatively low density and thus radiatively inefficient plasma. Overall, we do not expect the results presented in the following to be substantially affected by these simplifications.

3 JET PROPAGATION

We begin our analysis of AGN feedback with the propagation of a low-density jet of fixed luminosity. Jet propagation is a key aspect for feedback since the spatial deposition of feedback energy will be decisive for the jet's ability to impact cooling flows and not just heat the already hot, low-density outer ICM. We therefore hypothesize that jet propagation needs to be converged in order to obtain converged feedback effects from the jets. The general problem of jet propagation is already covered in Weinberger et al. (2017b), and the following section expands on this showing jets with higher resolution and in simulations with radiative cooling.

Fig. 3 shows a slice through the highest resolution jet simulation (*rw jet a 5*) at 25 Myr, i.e. when the jet shuts off. The main panel and the first zoom-in show the density, highlighting the cocoon

as well as the bow shock. The other two inlay panels show the component of the momentum flux density in jet direction transported in jet direction ($F_\parallel$, middle) and perpendicular to the jet direction ($F_\perp$, bottom), which highlight the jet propagation in the inflated cocoon. While the formation of the low-Mach number bow shock (Ehlert et al. 2018) is comparably simple to resolve and generic to outflows (Faucher-Giguère & Quataert 2012; King & Pounds 2015; Costa, Pakmor & Springel 2020), the contact discontinuity, i.e. the transition between shocked, dense material and shocked, underdense jet material forming a cavity, is prone to subsonic Kelvin–Helmholtz instabilities (KHI) and requires higher resolution. The extent to which these instabilities can grow depends on the ratio of the growth time to the dynamical time of the cavity itself, set by the buoyancy time-scale (Weinberger et al. 2017b). Resolving this mixing process between cavity and shocked ICM represents a significantly more difficult challenge computationally, since the relevant modes of the KHI need to be resolved.

Finally, the middle and lower panels show the jet as a collimated supersonic flow propagating in its cavity. Maintaining the momentum flux confined in a cylinder with diameter of only a few kpc is only possible if the velocity shear layer is resolved and if the hydrodynamic flow does not develop instabilities on time-scales shorter than the jet propagation time. In practice, this is the case if the flow is internally supersonic (see discussion in Padnos et al. 2018 and Mandelker et al. 2019, their section 2, as well as Berlok & Pfrommer 2019a, b for the magnetized case), and if the jet is resolved linearly by at least of the order of 10 cells per diameter, making this the most challenging aspect to model accurately in numerical simulations. If the outward momentum transport is not captured accurately in a numerical simulation, the respective position of the jet will be incorrect. Inverting this argument, a converged position of the jet head implies an accurate modelling of the momentum flux in the jet.[4] Note also that the propagation in this idealized setting with an initially spherically symmetric ICM density profile and constant jet luminosity is likely to lead to substantially larger travel distances and consequently more elongated cavities than comparable jets in cool-core galaxy clusters (Owen & Ledlow 1997).

We use the position of the jet at a given time as a measure of convergence of jet propagation, as shown in Fig. 4. It turns out that this seemingly simple criterion is non-trivial to achieve, even for hydrodynamic jets (Weinberger et al. 2017b; Yates, Shabala & Krause 2018), with jet distance generally increasing with increased resolution. Pushing the resolution in the jet further than in previous studies, however, we can see a turnaround in jet distance versus time plot with increasing resolution, in particular between *rw jet a 4* and *rw jet a 5* in Fig. 4. The colours indicate the different jet resolutions. Comparing the slices in Fig. 3 (which shows *rw jet a 5*) with the equivalent plot for *rw jet a 4* (Fig. A1), the most significant difference is the absence of body modes in the transverse momentum flux (bottom inlay panel) in the lower resolution run. We speculate that this momentum transport via transverse body modes of the KHI takes over the slowing down of the jet while it is dominated by numerical viscosity or numerical diffusion at lower resolutions.

4 EFFECT ON ICM

Having established the jet propagation and its behaviour with resolution, we now move on to study the effect of the jet event on

---

[4]Within the assumptions of an ideal gas. This certainly falls short to explain real AGN-driven jets.
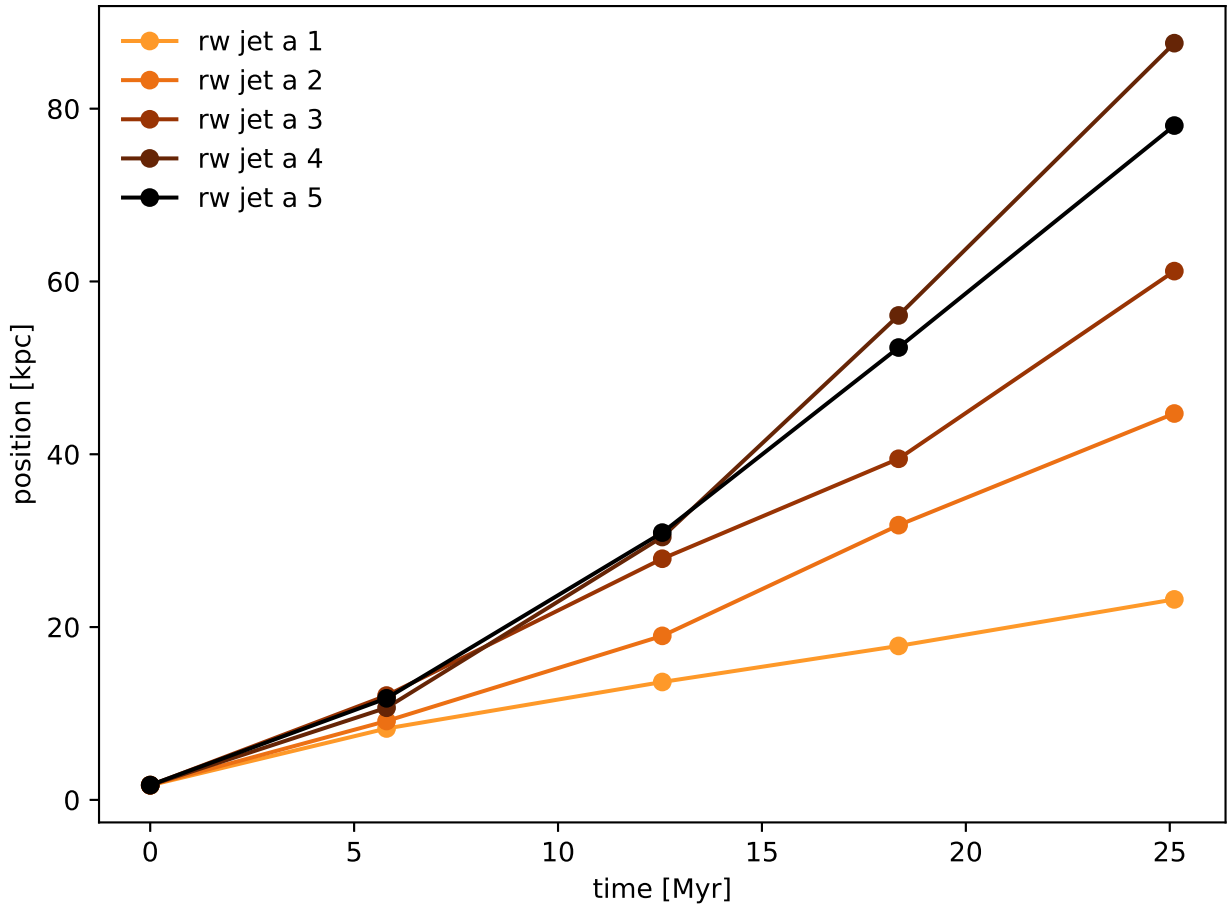
Figure 4. Jet position versus time for different jet and ICM resolutions. This shows that it is necessary to resolve the jet to resolution level 4, i.e. with resolution elements smaller than 100 pc for the jet propagation to be resolved.

the hydrostatic halo. We are particularly interested in the jet's ability to moderate or delay a developing cooling flow and its dependence on numerical and modelling aspects. For this purpose, we use the fixed luminosity jet simulations (as in the previous section) with a jet kinetic luminosity of 10^{45} erg s^{-1} for 25 Myr. These simulations include radiative cooling that allows us to study the effect of the jet on cooling times.

4.1 Numerical convergence of AGN jet feedback

Fig. 5 shows the gas mass-weighted cooling time distribution function for different jet resolutions and a reference run without a jet (black dashed line). All runs with jets cause a significant shift of the distribution function towards longer cooling times. *rw jet a 1* manages to shift it by 300 Myr, while starting at the resolution of *rw jet a 2*, the cooling time distribution function converges, being shifted by 400 Myr relative to the reference run. The radiated energy over 400 Myr (with cooling losses of the order of 10^{44} erg s^{-1}) corresponds to 1.3×10^{60} erg, which even slightly exceeds the injected energy, 0.8×10^{60} erg. This proves that jets with an average power that roughly matches the cooling luminosity are capable of delaying cooling flows. To determine the physical reason for this delay, we plot the phase diagram of the low-cooling time gas (<1 Gyr) in Fig. 6. Interestingly, the gas in the presence of jets is not hotter than the gas in the no jet case, but the high-density, high-pressure end is removed. Given the strong dependence of radiative cooling on density, it is not surprising that this leads to a substantial reduction
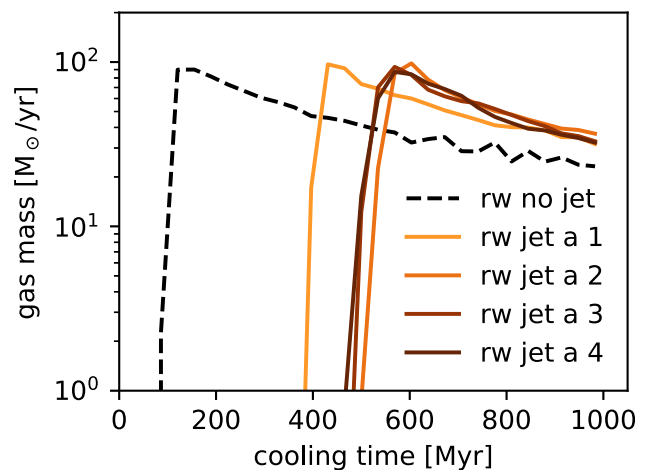

Figure 5. Gas cooling time histogram for different jet resolutions after 50 Myr. The 'preventive feedback' effects of jets, i.e. the delay of the developing cooling flow compared to the *no jet* simulation, are converged starting from the resolution of *rw jet a 2*, i.e. earlier compared to jet position.

in cooling luminosity and an absence of gas with short cooling times. We have thus shown that light hydrodynamical jets are able to efficiently delay developing cooling flows, mostly by removing the dense gas component. While the steep density dependence of
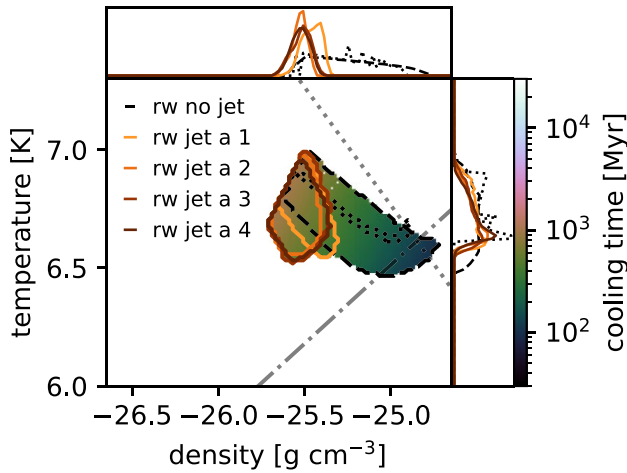
Figure 6. Phase diagram of cooling gas ($t_c < 1$ Gyr) for runs with different jet resolutions after 50 Myr. The dash–dotted line indicates an adiabat at 2 keV cm^2, and the dotted line indicates an isobar at 2×10^{-10} erg cm^{-3}. The reduction of cooling time is related to the boosting of the gas entropy, indicating an immediate response of the halo gas to the jet, rather than an isochoric temperature increase of the central gas. The black dotted contour shows the initial conditions.

the cooling time is the dominant factor for delaying the cooling flow, the removal of dense gas does involve non-adiabatic processes on the lowest entropy gas in the centre. Note that we do not make any statement about the energy coupling mechanisms to the ICM. However, these results suggest that the feedback effect of a jet after 50 Myr, i.e. 25 Myr after the jet shuts off, is not an isochoric heating process, i.e. an increased central gas temperature at fixed density, but already mediated by an increase in the entropy of the gas that reduces further cooling. Substantial increases in pressure and consequently strong shocks are absent at this point. We will closely examine the time evolution of the gas state at times <50 Myr in Section 4.3.

Examining the resolution dependence, it is particularly noteworthy that the thermodynamic effects on the ICM seem to converge at lower resolution than the jet propagation itself. This seemingly puzzling result can be easily illustrated with a map of the cooling times in the central cluster regions. Fig. 7 shows the cooling time at different times (columns) and for different resolutions (rows), with the last row showing an unmediated cooling flow for reference. Note that the middle column corresponds to the time when we analyse the cooling time distribution function in Figs 5 and 6. The low-cooling time gas is all centrally concentrated at distances smaller than the jet travel distance. Thus, the exact jet travelling distance has no immediate impact on the low-cooling time gas. The notable exception is *rw jet a 1*, where the jet is not able to break out of the inner region of cold gas at all.

What about the effect of resolution on the gas further out? Fig. 8 shows a mass-weighted two-dimensional (2D) histogram of cooling over free-fall time as a function of radius r. The free-fall time is defined as $t_{ff} = \sqrt{2\, r\, g^{-1}}$, with g being the radial gradient of the gravitational potential. The gas above the main ridge is the hot jet cocoon material and the different propagation behaviour between the models can be clearly identified in the left and central columns. Interestingly, however, this does not result in significantly different cooling over free-fall time distributions. In particular, the mass of gas outside 30 kpc with $t_c/t_{ff} < 10$ is converged to a few per cent

starting at *rw jet a 2*. Notably, the amount of cold gas in the outskirts increases due to the presence of a central jet, while the reference run develops a significant cooling flow and a factor of several higher cooling luminosities by 250 Myr, however, only in the centre. This effect is caused by substantial (ICM) gas outflows driven by the jet and the subsequent rising of the lobe (not explicitly shown here, but see e.g. Chen et al. 2019; Prasad, Voit & O'Shea 2022).

4.2 Sensitivity to modelling of jet feedback

Having shown numerical convergence, we now examine the dependence on different physical models for jets and AGN-driven outflows. For the model variations, we subsequently use resolution level 2 for which convergence has been established. Fig. 9 shows the cooling time distribution function for a variety of different models, in particular a jet with higher density (*rw jet d 2*), and an outflow with higher density and wide opening angle (*rw wind d 2*). For reference, we also compare this to the IllustrisTNG kinetic wind mode (*tng*) that acts via frequent momentum kicks of the central gas in a random direction.

Most notably, the impact of model differences is substantially larger than the resolution variations of *rw jet a* discussed in Fig. 5. The resolution effects of the *rw jet d* and *rw wind d* tend to be even smaller. This implies that the underlying modelling assumptions in the feedback model are the biggest source of uncertainty in this set-up (note that this set-up uses a fixed feedback power and duration and does not contain any complex multiphase gas). Looking at the individual simulations, there are a number of noteworthy trends. In particular, heavy jets have substantially weaker effects than light, low-density jets. This effect can be somewhat overcome by choosing an opening angle (*rw wind d 2*), yet the basic problem persists. The *tng* run exhibits a similar removal of low-cooling time gas as the light jet model. Fig. 10 shows the phase diagram of the gas with low cooling times for the different models. The ability to delay the cooling flow seems to correlate more with the absence of dense than with cold gas. *rw jet d 2* and *rw wind d 2* have a reduced ability to mediate the cooling flow. The *tng* model has a similar effect as *rw jet a 2* in this set-up.

To understand this outcome better, it is again useful to look at maps of the cooling time for the different runs, which are shown in Fig. 11. The similarity in cooling times of the *rw jet a 2* and *tng* models after 50 Myr (first and fourth rows, second column) originates from the ability of these models to clear the central gas. While this is done by kicks in random direction in *tng*, shocking the ICM and leaving behind a hot, long-cooling time post-shock gas, the key in the jet model is the cocoon of jetted material present in the centre, expanding outward perpendicular to the jet direction to adjust to the jet-induced overpressure. This increases the entropy of the low-cooling time gas and moves it to larger radii and lower pressure environments, thereby increasing its cooling time. Importantly, this material is not present if the jet is heavier (i.e. having a higher momentum flux at fixed energy) because in this case, the jet is able to drill through the ICM and consequently very little jetted material remains in the centre, leading to a less efficient delay of the cooling flow (qualitatively consistent with the scaling of the cocoon width described in Su et al. 2021). A wider opening angle (*rw wind d 2*) leads to an earlier stopping, but does not fully overcome the effect. It should be noted, however, that the jet density is not the only factor of importance. In particular, simple analytical considerations of momentum density balance in the jet head rest frame (see e.g. Begelman,
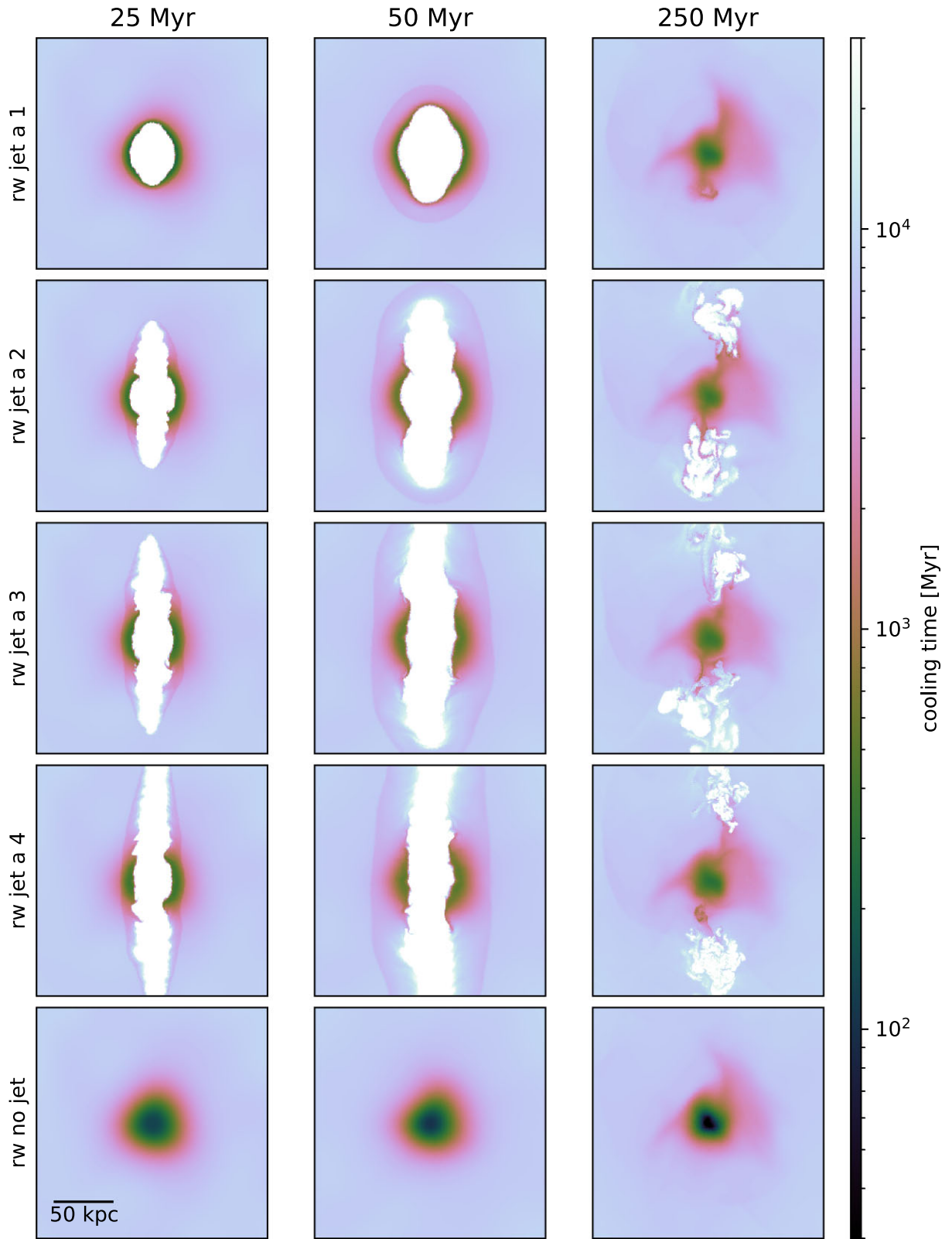
Figure 7. Slices of the cooling time of simulations with different jet resolutions (rows) after 25, 50, and 250 Myr (columns). The maps show a region of 200 kpc side length. The last row shows a simulation without a jet, for reference. Except for the lowest jet resolution (*rw jet a 1*), the effects of the jet on cooling time are very similar due to similar behaviours in the central region, despite different jet propagation further out.
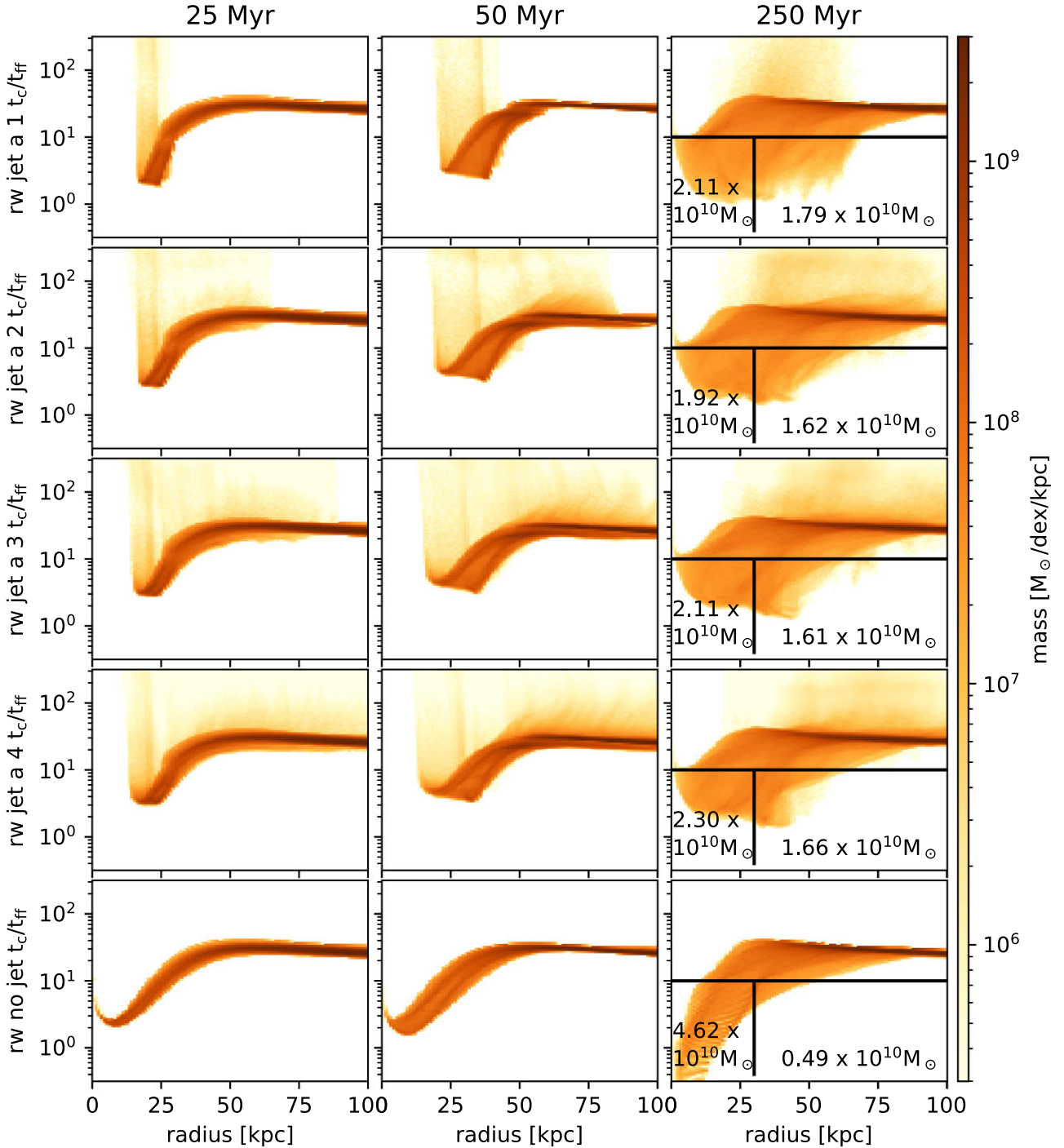
Figure 8. 2D histogram of cooling over free-fall time as a function of radius for different jet resolutions.

Blandford & Rees 1984) yield a speed at which the jet head advances (v_a) of

$$v_a = (1 - (\rho_e/\rho_{jet})^{1/2})^{-1} v_{jet} \approx \left(\frac{\rho_{jet}}{\rho_e}\right)^{1/2} v_{jet}$$

$$\approx \left(\frac{2\dot{E}}{A\rho_e}\right)^{1/3} \left(\frac{\rho_{jet}}{\rho_e}\right)^{1/6}, \tag{22}$$

where we assume that the external density $\rho_e \gg \rho_{jet}$ and use equation (11) to replace v_{jet} with the jet kinetic luminosity $\dot{E}$. Equation (22)

highlights the importance not just of the jet density, but also the external density ρ_e, jet kinematic luminosity $\dot{E}$, and cross-section A to influence the behaviour, yet they are left constant in this study. A multiphase external medium and entrainment further complicate the picture (Mukherjee et al. 2016). The weak dependence of the jet head advance on jet density in equation (22), however, does not imply a weak dependence on heating of the surrounding ICM. The lateral extent of the cavity does depend more strongly on jet density [see e.g. Su et al. 2021, their equation (10) for a simple
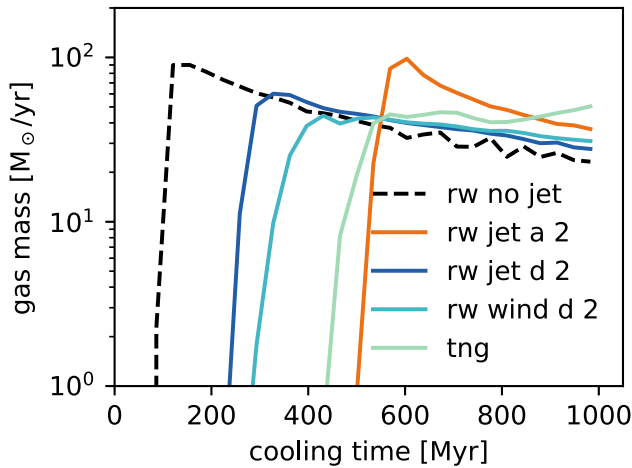
Figure 9. Same as Fig. 5, only with different AGN feedback models after 50 Myr. The ability to alter the cooling time PDF, and consequently the ability to moderate cooling flows, is highly model and parameter dependent. The resolution effects for the *rw jet d 2* are smaller than those for the light jet indicated in Fig. 5 (not shown).
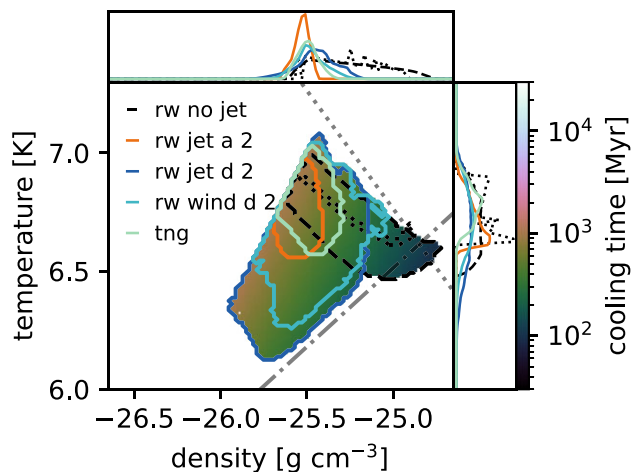

Figure 10. Same as Fig. 6 but comparing the simulations with varying model parameters.

model]. Related to this effect, we find the bow-shock Mach number in directions perpendicular to the jet to be increased for lighter jets, leading to increased shock heating of the ICM in this direction. For a more detailed discussion on how jet parameters impact cocoon formation, see Su et al. (2023). Having a look at the longer term effect of the cooling over free-fall time distribution (Fig. 12), there is again a strikingly universal increase in cold gas at larger radii for the models that are able to reduce the cooling times most efficiently.

We conclude from this part that the choice of parameters of the feedback model has a larger impact than resolution effects for this set-up. Interestingly, very light jets have a similarly strong effect on cooling times after 50 Myr as the kinetic feedback mode in the IllustrisTNG simulation, while models with heavier jets or directional winds are less efficient due to their reduced ability to affect the innermost ICM gas.

4.3 Differences due to hydrodynamics code and implementation

The large differences for runs with different models and parameters we studied in the last subsection prompt the question of how comparable runs with independent codes are, as they employ different hydrodynamics solvers, different cooling functions, and a different parametrization and implementation of the feedback source terms. To study this, we compare the simulations similar to the ones presented so far to equivalent (see Section 2.2.2) ones employing the Su et al. (2021) jet model (*kys jet b* and *kys jet c*) that uses the GIZMO code, a meshless finite mass hydrodynamics solver, and the FIRE-2 model for cooling. Note that the model parameter variations in this subsection are less extreme than in the previous one to allow a comparison across implementations.

Fig. 13 shows the cooling time distributions for different codes, each one with two parameters controlling for different momentum fluxes (model *b* with lower jet momentum flux, i.e. lower jet density and higher velocity, model *c* with higher momentum flux). The reference run without jet (dashed black line) differs at the low-cooling time end. This can be explained by the fact that the cooling model in the AREPO simulation cuts off at 10^4 K, thereby de facto imposing a lower limit to the cooling time (at this point, the star formation model takes over). The FIRE-2 model follows the thermal instability explicitly to lower temperatures, thus populating the low-cooling time distribution function. We speculate that the noise in the distribution function is due to details of the numerical implementation of the cooling and will not be considered further in this work. For the simulations including jets, two features are noteworthy: first, the two codes produce different cooling time distributions, the *kys* implementation being less able to delay the cooling flow in this set-up. Secondly, parameter *b* creates a larger delay in cooling time compared to parameters *c* for both models.

In order to explore the origin of the differences between the different codes, it is again useful to examine the phase diagram of the cooling gas. Fig. 14 shows this phase diagram, this time not only after 50 Myr as in previous plots (bottom), but also while the jet is active (top after 12.5 Myr, centre after 25 Myr). The overall response of the gas to an active jet after 12.5 Myr is an increase in pressure (shift to the top right), with an accompanying increase in entropy (shift to the top left). The former seems to be universal across codes and parameters, while the latter is more model and parameter dependent. Once the halo gas has time to hydrodynamically respond to the changed conditions, the gas expands adiabatically, decreasing its pressure while changes in entropy are more and more driven by cooling.

The large differences in the cooling time distribution function after 50 Myr seem to be gradually developing, with differences at earlier times being much smaller. This indicates that the substantial differences in outcome between codes originate from diverging evolution of the cooling flow given small differences induced by the different jet models and by differences in the cooling functions. The response of the gas to a jet with fixed energy is qualitatively similar, though a lower efficiency of the *kys jet* implementation (and of the lower density jet model *c* relative to model *b* at fixed implementation) is already visible after 12.5 Myr. This implies that both model parameter choices and the specific implementation are sources of uncertainty that can, due to the non-linearity of the developing cooling flow, lead to divergent results at fixed energy injection.

The cooling time maps of the simulations with different codes are shown in Fig. 15. In terms of jet propagation, the two models look remarkably similar. The *rw jet* models have more pronounced bow
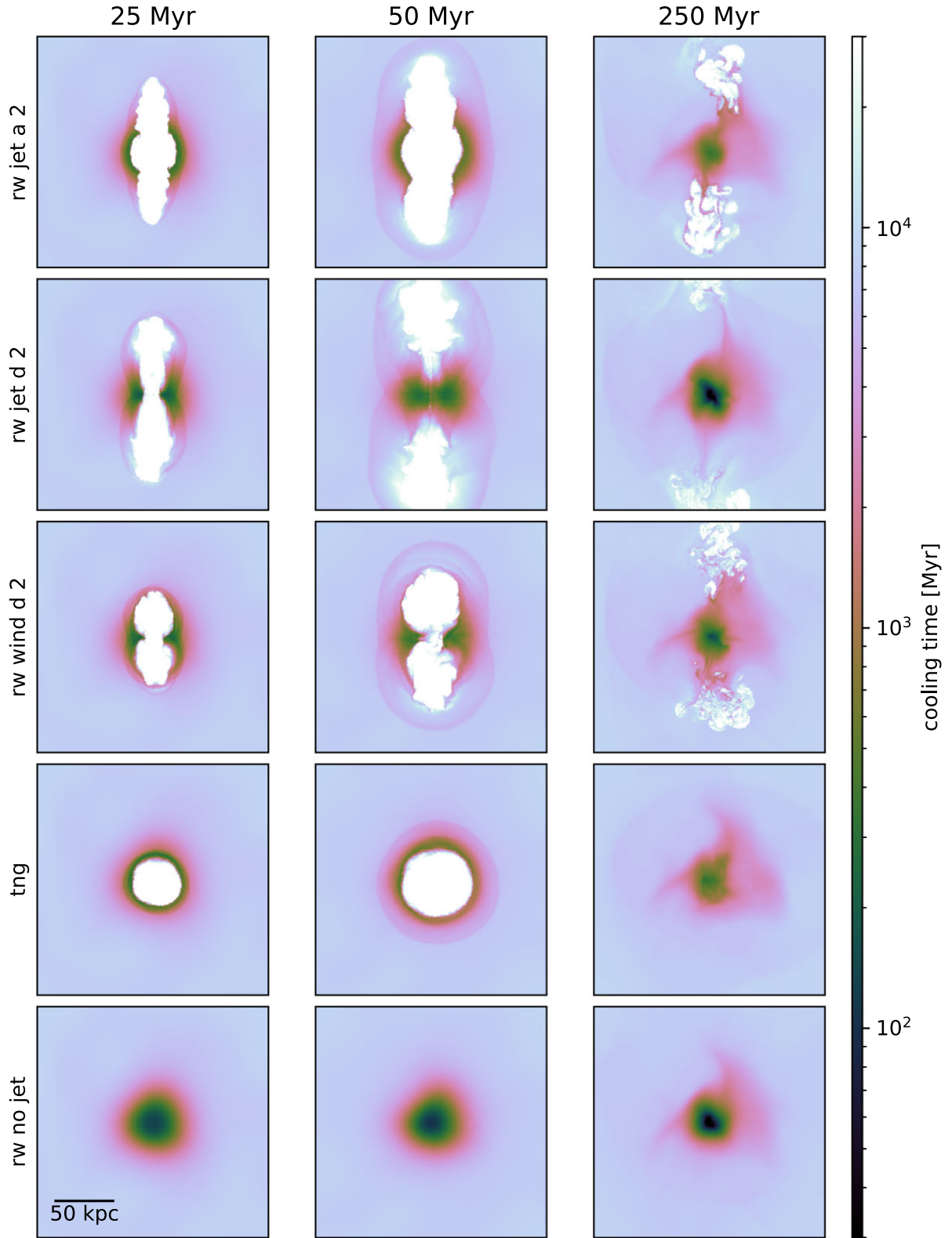
Figure 11. Same as Fig. 7, but for simulations with different jet parameters and feedback models. The last row shows the simulation without feedback. The inefficiency of *rw jet d 2* to offset cooling flows seems to originate from its inability to affect the central gas.
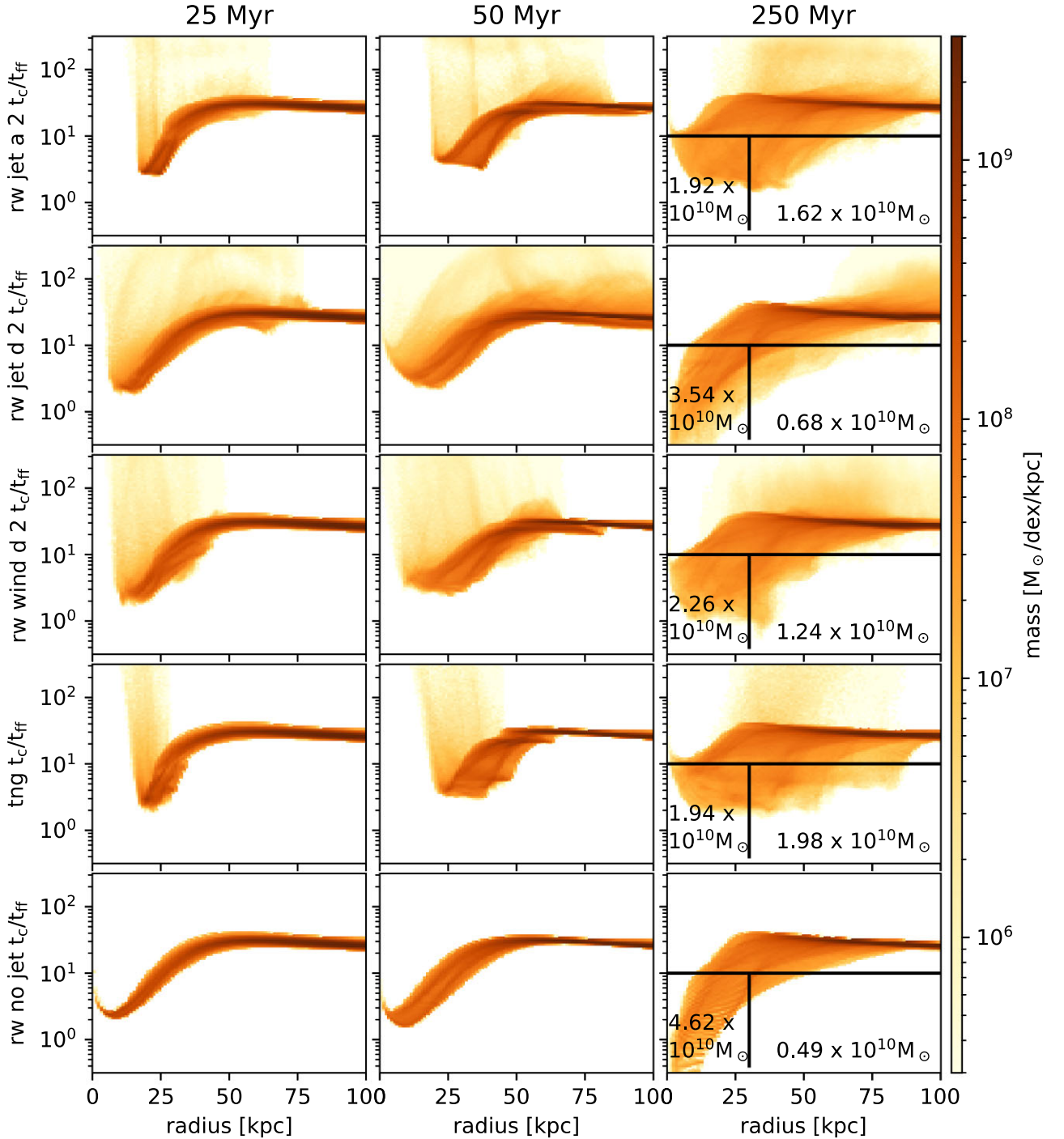
Figure 12. 2D histogram of cooling over free-fall time as a function of radius for different AGN-driven jet and wind models.

shocks (visible in the cooling time map), indicating that the difference in entropy change could be due to differences in shock heating. This could be caused by details of the jet injection algorithm or due to the different hydrodynamics solver. Towards later times, after 250 Myr, the *rw jet* simulations, i.e. the ones run with AREPO, show a stronger tendency to shatter the jet-inflated cavity (an effect that would be suppressed if magnetic fields were present). Trends in cooling over free-fall time are similar to the ones discussed in Section 4.2 and shown in Appendix B.

Overall, we conclude that differences in code, cooling function, and model parameters far exceed resolution effects and uncertainties due to numerical (non-)convergence. This, in combination with the code-independent trend of heavy/kinetic versus light/thermal jets, implies that jet modelling needs to be improved in two regimes to increase the reliability of AGN feedback modelling in galaxy cluster simulations: first, a more detailed knowledge about the physical conditions in jets and secondly, constraints from smaller scale jet simulations about the effect at injection scales in order to establish
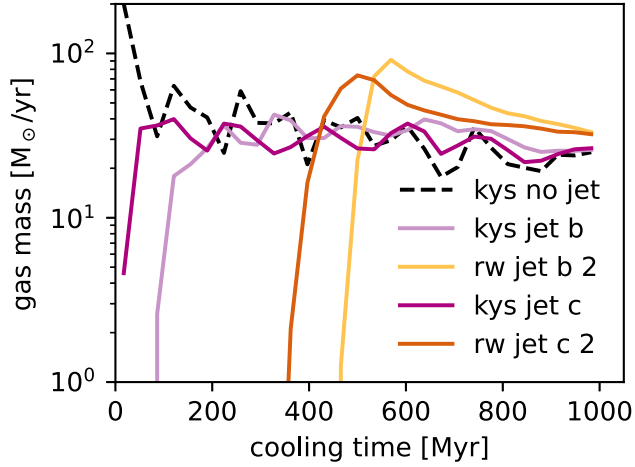
Figure 13. Same as Fig. 5, only with different AGN feedback model and run with a different code, cooling and star formation model. Simulations starting with *kys* use the meshless finite mass mode of the GIZMO code, while simulations starting with *rw* employ a finite-volume moving mesh solver using AREPO. The ability to alter the cooling time PDF, and consequently the ability to moderate cooling flows, is highly code as well as model parameter dependent.

a 'correct' way to inject a jet in lower resolution galaxy cluster simulations. Finally, it is important to note that the presented set-up of a fixed energy output, while instructive, is artificial since simulations of galaxy cluster evolution require a self-regulated accretion-feedback set-up. This self-regulation will likely act as an attractor towards a steady-state solution with global heating–cooling balance, thereby reducing the differences discussed in this section.

5 SELF-REGULATED RUNS

Having established the ability of jets to delay developing cooling flows, and their resolution convergence requirements, we now focus on the more complex case of a self-regulated set-up, where the jet kinetic luminosity $\dot{E}$ is coupled to the accretion rate via a fixed efficiency:

$$\dot{E} = \epsilon_{f,kin} \dot{m}_{acc} c^2, \qquad \epsilon_{f,kin} = 0.1. \qquad (23)$$

The accretion rate $\dot{m}_{acc}$ is estimated using the Bondi formula and c denotes the speed of light. For a self-regulated cooling–heating equilibrium state to be reached, the simulated time needs to be extended to several times the central cooling time. We perform the simulations for 2 Gyr as a compromise, allowing an equilibrium situation to be established, yet the assumption of an isolated halo, i.e. the omission of cosmological accretion, is still a reasonable approximation of the ICM in a galaxy cluster. We compare three simulations in this section: a run without AGN feedback as a reference for a cooling flow, a run with the *rw jet* model, and a run with the *tng* kinetic feedback model. Note that we restrict the comparison in this section to simulations run with AREPO and the jet parameters to model *a*. A comparison to denser jets in a self-regulated set-up is presented in Ehlert et al. (2023). The black hole masses in the latter two simulations are chosen such that the resulting equilibrium star formation rates are similar, and can be considered free parameters in this set-up. In particular, we note that the black hole mass in the *tng* model is 3×10^9 M$_\odot$, while it is only 3×10^8 M$_\odot$ for the *jet* model. This has the practical consequence that the accretion rate of the *tng* simulation is boosted by a factor of 100 compared to
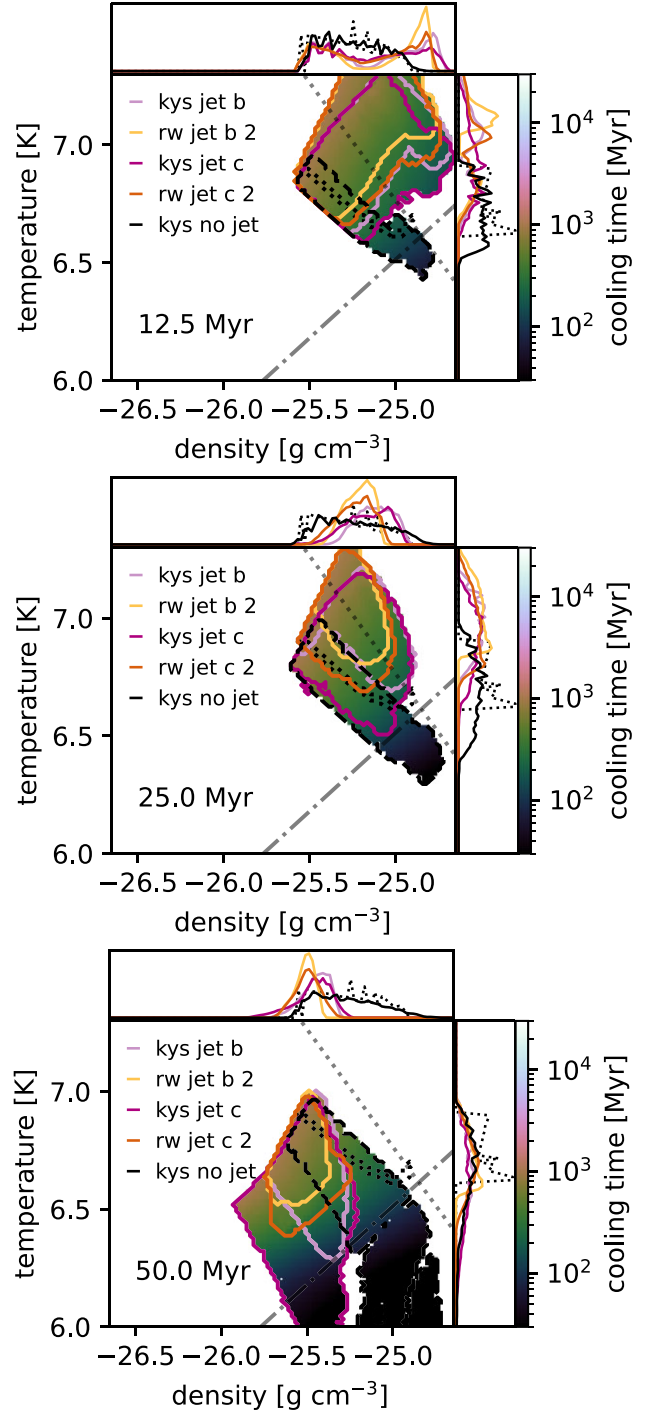

Figure 14. Phase diagram of gas with short cooling time after 12.5 Myr (top), 25 Myr (middle), and 50 Myr (bottom) for simulations with different models and using different simulation codes. Simulations starting with *kys* use the meshless finite mass mode of the GIZMO code, while simulations starting with *rw* employ a finite-volume moving mesh solver using AREPO. The increased difference in gas distribution between the different codes at later times indicates the role of the different cooling functions and the non-linearity of the developing cooling flow.
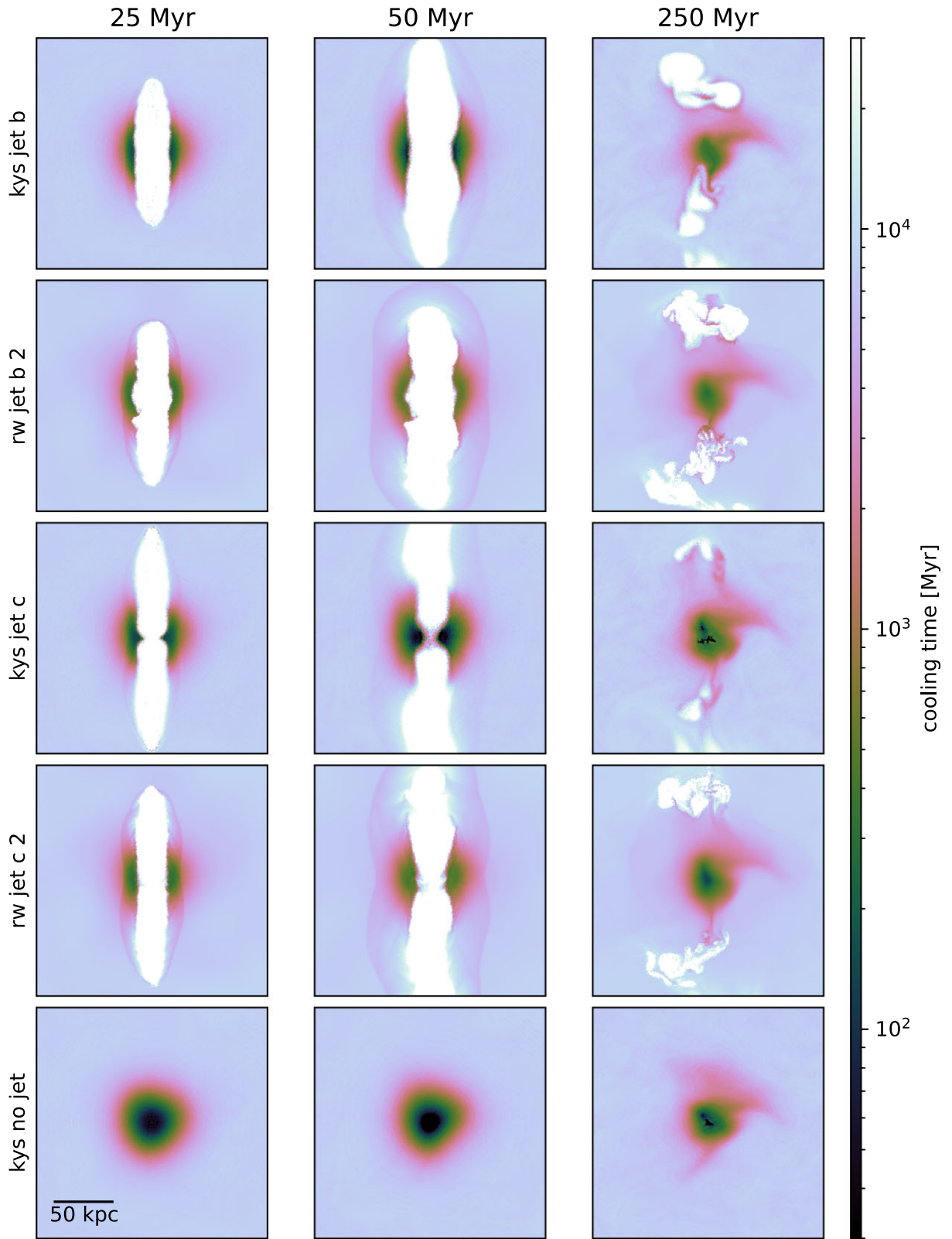
Figure 15. Same as Fig. 7, but for simulations with different codes and jet implementations. Simulations starting with *kys* use the meshless finite mass mode of the GIZMO code, while simulations starting with *rw* employ a finite-volume moving mesh solver using AREPO. The last row shows the simulations without feedback (GIZMO version).
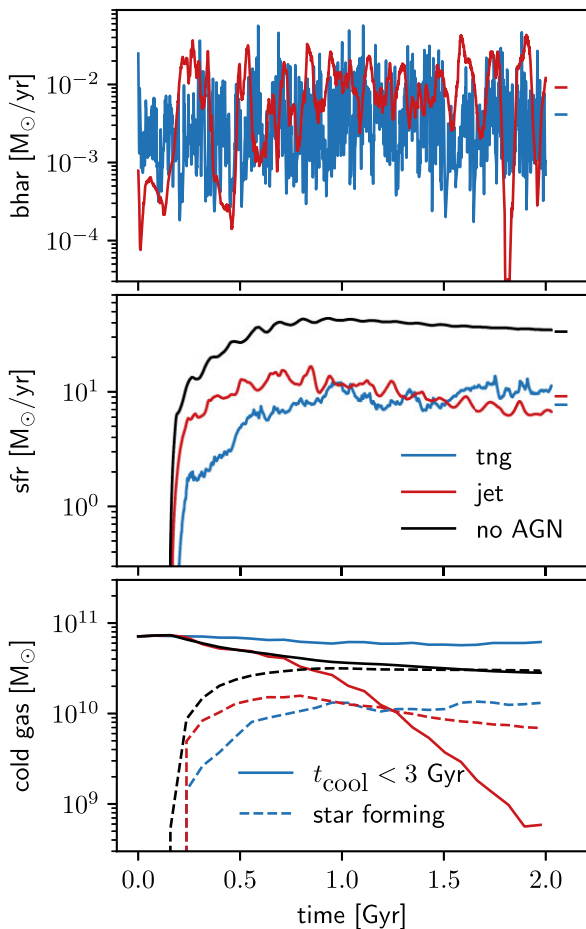
Figure 16. Black hole accretion rate, star formation rate, and cooling (solid) and star-forming (dashed) gas mass as a function of time for different AGN feedback models run with the AREPO code. While the *tng* model acts on the star-forming gas and the immediate surroundings, the *jet* model acts on the cooling, not yet star-forming gas, leading to a different time variability.

the *jet* simulation, assuming the same surrounding gas density and sound speed. If we were to run the *tng* simulation with $3 \times 10^8 \, M_\odot$, the feedback would keep the black hole accretion rate at a relatively moderate rate; however, it would not be able to suppress the overall star formation rate over the entire 2 Gyr run time. With the different masses in place, we are able to obtain simulations with comparable levels of star formation and black hole accretion, but necessarily with very different central gas densities and sound speeds. The origin of this behaviour will become clearer once we discuss the runs in more detail.

We start by showing the time evolution of the black hole accretion rate, the star formation rate, and the mass in star-forming and rapidly cooling (cooling time $t_c < 3$ Gyr, but not yet star-forming) gas in Fig. 16. First, as seen in the middle panel, the *tng* run shows almost an order of magnitude reduced star formation relative to the run without AGN feedback. Interestingly, the rate of star formation is reduced by a similar degree in the *jet* run, yet with somewhat different time evolution. We note that the level of agreement (time averages as horizontal lines at 2 Gyr) is secondary since we have chosen different black hole masses in the two simulations. It is remarkable that light jets can mediate the cooling flow to similar levels of star formations as *tng*. The black hole accretion rate shown in the top

panel is comparable between the two models, with only a slightly higher overall accretion rate for the jet model. This implies that the total injected energy via AGN feedback is comparable between the two runs as well.

The bottom panel of Fig. 16 shows the rapidly cooling (solid) and cold, star-forming (dashed) gas components in the different simulations. While the star-forming gas closely follows the star formation rate, which is a direct consequence of the employed Springel & Hernquist (2003) multiphase ISM sub-grid model, the cooling, but not yet star-forming gas masses differ drastically: the gas mass in rapidly cooling gas in the *no AGN* run decreases likely due to transitioning to the star-forming gas phase and ultimately forming stars. Surprisingly, the *tng* run is able to retain more mass in rapidly cooling gas. The *jet* simulation, on the other hand, initially follows the *no AGN* run, builds up a star-forming gas reservoir that is a factor of a few larger than that in *tng* (but still lower than the *no AGN* case), and from 0.75 Gyr onward slowly depletes the star-forming phase. More prominently, it also drastically depletes the rapidly cooling phase, in the end by two orders of magnitude. This implies that, while the run applying the *tng* model appears to reach a steady state, the run using AGN-driven jets undergoes a transformation on Gyr time-scales (while being self-regulated in terms of smaller scale star formation and black hole accretion rate). In summary, we have two self-regulated isolated galaxy cluster simulations employing different AGN feedback models, injecting similar amounts of energy into the system, leading to a similar overall star formation suppression, yet a completely different evolution of the rapidly cooling gas, indicating that the mechanism by which they suppress star formation is fundamentally different.

To better understand how the feedback models act differently on the gas, we show the gas density, temperature, and cooling time as a function of radius in 2D histograms in Fig. 17, left-hand panel, and the respective distribution functions in the right-hand panels. We choose to show the distributions at a time well into the simulations, after the runs start to visibly diverge. The density distributions (top panels) clearly show a bimodality of dense, central (and by definition) star-forming gas and lower density halo gas. While the bimodality exists in both simulations, the run of the *jet* model completely lacks gas in between the two peaks. By contrast, there is gas in between the two density peaks for the *tng* run. A similar trend is seen in temperature (central panel), where the hot gas corresponds to the halo, and a tail towards lower temperatures is only present in the *tng* run. The combination of the higher density and lower temperature of this 'transition' phase leads to gas with substantially reduced cooling times (bottom panel) in the *tng* simulations. Note that in this panel, the star-forming gas is not present since this quantity loses its meaning once the gas is in the star-forming phase, i.e. on an effective equation of state. We showed that the jet model is able to deplete the 'transition gas', which is able to rapidly cool and join the star-forming phase. While this undoubtedly leads to a reduction of star formation, we cannot exclude a direct impact of the jet on the star-forming phase, however to a lesser degree than in the IllustrisTNG model.

Finally, we focus on one of the consequences of the different ways the feedback models act on the halo gas. In particular, we consider the time variability of the black hole accretion rate and the star formation rate as shown in Fig. 16. By eye, it is already clear that the *tng* run shows a significantly higher degree of high-frequency time variability than the *jet* run. This is most clearly visible in the black hole accretion rate. To quantify the variability time-scales, we use the logarithmic black hole accretion and star formation rates in the
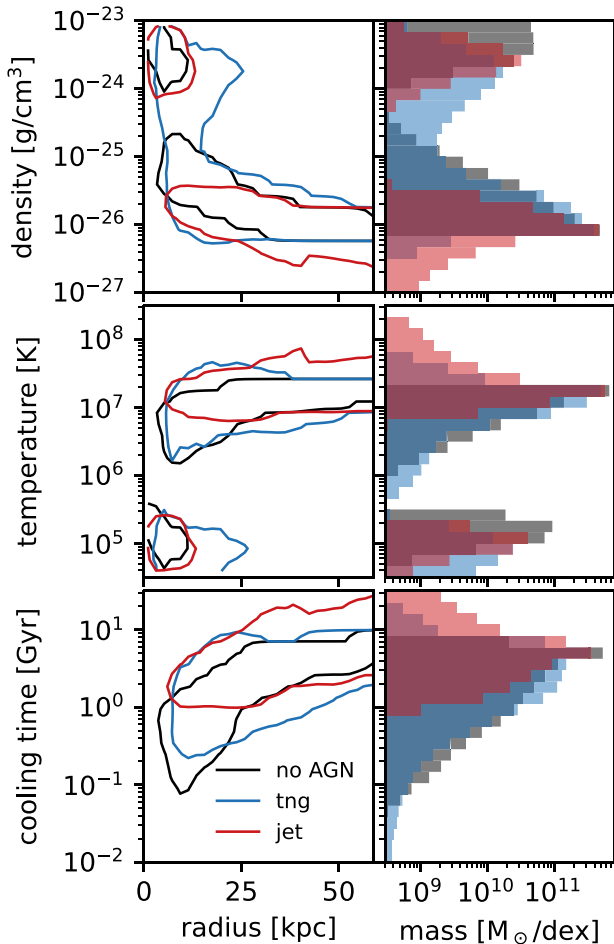
Figure 17. Gas density, temperature, and cooling time as a function of radius after about 1.18 Gyr. The *jet* model clearly reduces the density of the hot, dilute component more than the *tng* model, leading to longer cooling times, while leaving a dense, star-forming component in place. The contour is located at values of 10^8 $M_\odot$ kpc^{-1} dex^{-1}.

second half of the simulation time (1–2 Gyr), subtract a linear fit,[5] and normalize their amplitude to further analyse the signal (Fig. 18, left). We then calculate its power spectrum and overplot roughly matching power-law scalings in Fig. 18, right. While the power of the black hole accretion rate scales with the inverse frequency in the *tng* run, the *jet* run shows a τ^3 scaling; i.e. the accretion rate is by far dominated by a larger variability time-scale up to a time-scale of ~100 Myr. It is reasonable to assume that the variability on the larger time-scales is more connected to hot halo properties, while more power on smaller time-scales is connected to the ISM, making this result qualitatively consistent with the notion that the *tng* model acts more on the ISM, while the *jet* acts predominantly on the hot halo. Interestingly, this trend also carries over to the time-variability signal in the star formation rate in these haloes, presenting a potential avenue to distinguish the two models (see e.g. Iyer et al. 2020; Tacchella, Forbes & Caplar 2020). The power spectrum of the star formation rate falls off more steeply than that of the accretion rate, indicating a lower degree of variability on small time-scales, likely due to star formation happening on larger spatial scales and

[5]This is done to remove potential effects originating from star-forming gas depletion over Gyr time-scales that are unrealistic due to our isolated set-up.

being only indirectly (via the injected feedback energy) coupled to the black hole accretion rate.

6 DISCUSSION AND CONCLUSION

In this paper, we examine simulations of hydrodynamical jets propagating into an isolated, radiatively cooling halo. For simulations that couple jet power to the accretion rate, we find the following:

(i) Light hydrodynamic jets can suppress cooling flows. This differs from some early numerical studies (Vernaleo & Reynolds 2006; Cattaneo & Teyssier 2007), but more in line with more recent, higher resolution studies (e.g. Li et al. 2017; Beckmann et al. 2019). Unlike these studies, in our simulations neither jet precession nor an opening angle is required, likely due to higher jet velocities/lower momentum fluxes/lower mass loading at fixed jet kinetic luminosity (Omma et al. 2004; Dubois et al. 2010; Li & Bryan 2014; Ehlert et al. 2023).

(ii) Unlike the kinetic wind feedback in IllustrisTNG, collimated low-density jets predominantly act on the hot phase, reducing the amount of gas that is about to cool, while leaving the cooler, star-forming gas phase intact. This difference in feedback explains the need for different 'normalizations' in the Bondi formula (i.e. different black hole masses or efficiency factors) for the two models to maintain a self-regulated equilibrium state.

(iii) The different ways feedback acts lead to clear differences in the time variability in both black hole accretion rate and star formation rate. Jet feedback tends to lead to a time variability scale of 100 Myr, while wind feedback has a substantial time variability on even shorter time-scales. Note that the variability in the (light) jet case is increased compared to self-regulated simulations with heavier jets (see Gaspari et al. 2011; Ehlert et al. 2023).

Using simulations that cover only the onset of the cooling flow and fixed jet kinetic luminosity, we show the following:

(i) The delay of the cooling flow on 50 Myr time-scales is mostly achieved by heating and increasing the entropy of the densest gas of the hot atmosphere located in the very centre, thereby reducing the cooling luminosity.

(ii) Light jets achieve this via their expanding cocoon perpendicular to the jet propagation direction, pushing the ICM gas to larger radii and lower pressure environments. This is consistent with Cielo et al. (2014, 2017), finding that backflows of jetted material have a substantial impact on the gas surrounding the black hole already after several Myr. While the entropy of the ICM gas increases, the system reacts to the jet-induced overpressure quickly by expanding and the temperature returns the same levels it started out within a fraction of the central cooling time.

(iii) The response of the halo to a fixed-luminosity jet is similar for different numerical methods (AREPO versus GIZMO) and jet injection implementations (Weinberger et al. 2017b versus Su et al. 2021). Yet, small differences in jet and cooling function can be amplified and lead to diverging results over time.

(iv) Heavier jets tend to propagate outwards faster, diminishing their effect on gas in the very centre. Hence, they have a smaller impact on the cooling time distribution of the most rapidly cooling gas. We find this trend independent of code and implementation details.

(v) The more efficient feedback models tend to produce more thermally unstable gas ($t_c/t_{ff} < 10$) at large radii (>30 kpc). The reason for this might be twofold: first, due to outflow of low-entropy gas (Chen et al. 2019), and secondly, due to a prevention of radial
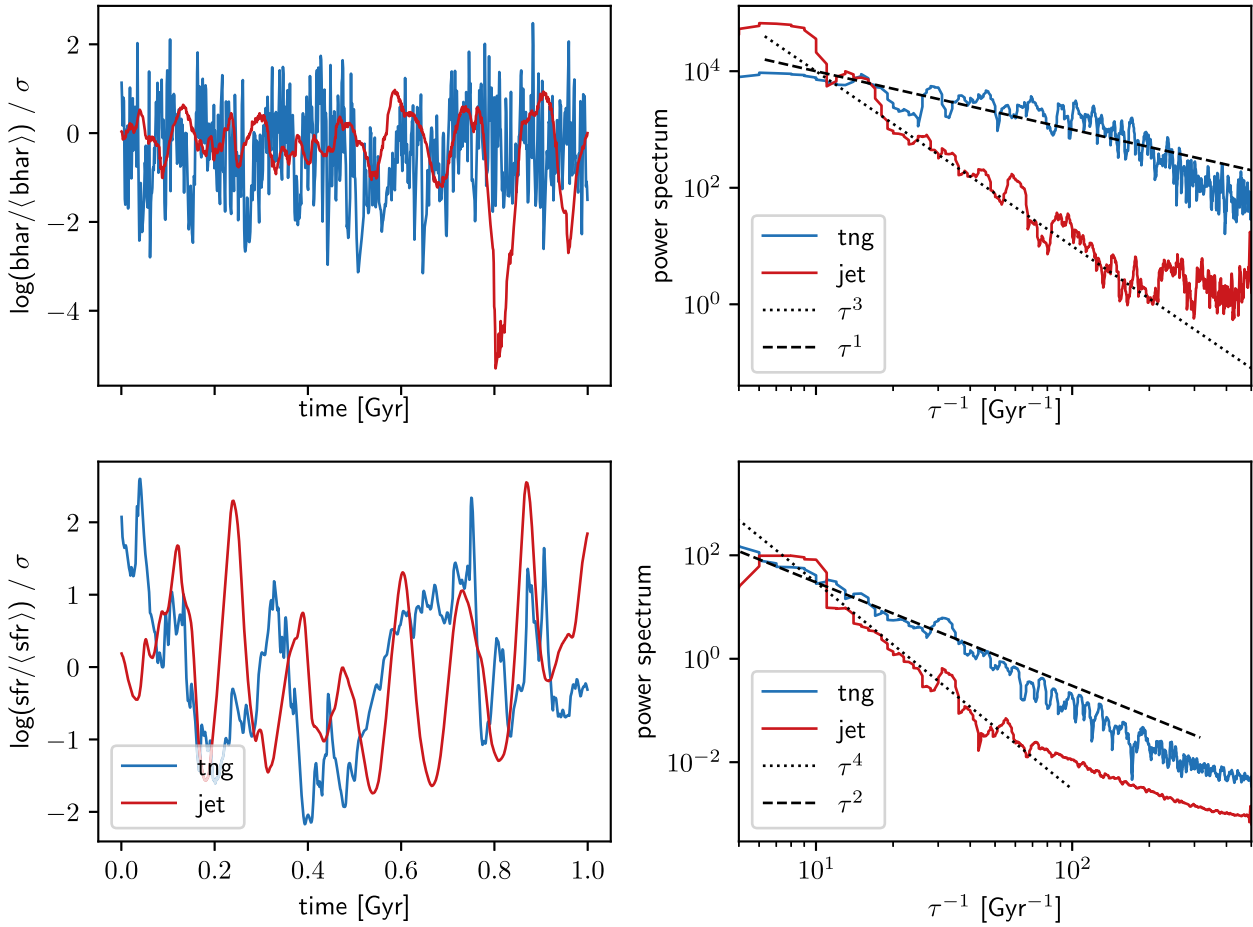
Figure 18. Left: Normalized black hole accretion rate (top) and star formation rate (bottom) of self-regulated runs using *tng* and *jet* feedback. The rates are extracted from 1 to 2 Gyr in the simulations, a linear fit to the respective quantity [log(sfr), log(bhar)] is subtracted, and the resulting rate is normalized by its standard deviation. Right: Power spectra of the respective rates. Both the accretion rate and the star formation rate have larger high-frequency power for the *tng* run, while the spectra decline more steeply for the *jet* run.

inflow of cooling gas: in the pure cooling flow case, the pressure support disappears first in the centre, allowing a radial inflow on time-scales smaller than the cooling time. This leads to gas being transported to the centre before the thermal instability fully develops. If the central pressure support is maintained due to AGN feedback, the thermal instability might develop at larger radii, leaving more gas with low t_c/t_{ff} ratios at larger radii.

(vi) The ability of jets to delay cooling flows is converged at moderate jet resolutions. In particular, convergence of feedback effects does not require convergence in jet propagation.

(vii) Jet propagation ultimately converges provided the diameter of the jet is sufficiently resolved.

(viii) Different parameters and models for the jets have varying ability in delaying cooling flows. This implies that the largest uncertainty remaining is the choice of the model and its parameters, and not numerical (i.e. resolution) limitations.

These results highlight the non-uniqueness of AGN feedback implementations for 'solving' the cooling flow problem. We suggest using signatures directly related to jets and AGN feedback such as properties of X-ray cavities (Bîrzan et al. 2020) to distinguish between mechanisms in future work.

One notable shortcoming of this set of simulations is the absence or overly simplified treatment of the multiphase ISM surrounding

the jet (Cielo et al. 2018; Mukherjee et al. 2018; Tanner & Weaver 2022). The presence of cold gas clumps could potentially alter the short-term variability of star formation in the *jet* run (Mandal et al. 2021). For current models, it is challenging to model the ISM structure accurately yet cover a simulation time of several Gyr, but new numerical approaches (Weinberger & Hernquist 2023) might be able to overcome this problem in the future.

Using the results presented here, it is possible to use this predictive model of AGN jet feedback at the required resolution for numerical convergence in more realistic set-ups. This includes more massive analogues of local galaxy clusters in isolation (Ehlert et al. 2023) and cosmological zoom simulations.

ACKNOWLEDGEMENTS

DATA AVAILABILITY

The data underlying this article will be shared on reasonable request to the corresponding author.

REFERENCES

Bambic C. J., Reynolds C. S., 2019, ApJ, 886, 78
Barnes D. J. et al., 2019, MNRAS, 488, 3003
Beckmann R. S. et al., 2019, A&A, 631, A60
Begelman M. C., Blandford R. D., Rees M. J., 1984, Rev. Mod. Phys., 56, 255
Berlok T., Pfrommer C., 2019a, MNRAS, 485, 908
Berlok T., Pfrommer C., 2019b, MNRAS, 489, 3368
Bicknell G. V., 1994, ApJ, 422, 542
Bicknell G. V., 1995, ApJS, 101, 29
Bîrzan L. et al., 2020, MNRAS, 496, 2613
Bîrzan L., Rafferty D. A., McNamara B. R., Wise M. W., Nulsen P. E. J., 2004, ApJ, 607, 800
Bourne M. A., Sijacki D., 2017, MNRAS, 472, 4707
Bourne M. A., Sijacki D., 2021, MNRAS, 506, 488
Bourne M. A., Sijacki D., Puchwein E., 2019, MNRAS, 490, 343
Bower R. G., Benson A. J., Malbon R., Helly J. C., Frenk C. S., Baugh C. M., Cole S., Lacey C. G., 2006, MNRAS, 370, 645
Cattaneo A., Teyssier R., 2007, MNRAS, 376, 1547
Chatterjee K., Liska M., Tchekhovskoy A., Markoff S. B., 2019, MNRAS, 490, 2200
Chen Y.-H., Heinz S., Enßlin T. A., 2019, MNRAS, 489, 1939
Churazov E., Sunyaev R., Forman W., Böhringer H., 2002, MNRAS, 332, 729
Cielo S., Antonuccio-Delogu V., Macciò A. V., Romeo A. D., Silk J., 2014, MNRAS, 439, 2903
Cielo S., Antonuccio-Delogu V., Silk J., Romeo A. D., 2017, MNRAS, 467, 4526
Cielo S., Bieri R., Volonteri M., Wagner A. Y., Dubois Y., 2018, MNRAS, 477, 1336
Costa T., Pakmor R., Springel V., 2020, MNRAS, 497, 5229
Croton D. J. et al., 2006, MNRAS, 365, 11
Duan X., Guo F., 2020, ApJ, 896, 114
Dubois Y., Devriendt J., Slyz A., Teyssier R., 2010, MNRAS, 409, 985
Ehlert K., Weinberger R., Pfrommer C., Pakmor R., Springel V., 2018, MNRAS, 481, 2878
Ehlert K., Weinberger R., Pfrommer C., Pakmor R., Springel V., 2023, MNRAS, 518, 4622
English W., Hardcastle M. J., Krause M. G. H., 2016, MNRAS, 461, 2025
Fabian A. C., 2012, ARA&A, 50, 455
Fanaroff B. L., Riley J. M., 1974, MNRAS,167, 31
Faucher-Giguère C.-A., Quataert E., 2012, MNRAS, 425, 605
Fujita Y., Cen R., Zhuravleva I., 2020, MNRAS, 494, 5507
Gaspari M., Brighenti F., D'Ercole A., Melioli C., 2011, MNRAS, 415, 1549
Gaspari M., Brighenti F., Temi P., 2012, MNRAS, 424, 190
Gaspari M., Temi P., Brighenti F., 2017, MNRAS, 466, 677
Genel S. et al., 2014, MNRAS, 445, 175
Guo F., 2016, ApJ, 826, 17
Guo F., Oh S. P., 2008, MNRAS, 384, 251
Hardcastle M. J., Croston J. H., 2020, New Astron. Rev., 88, 101539
Hardcastle M. J., Krause M. G. H., 2014, MNRAS, 443, 1482
Hillel S., Soker N., 2017, ApJ, 845, 91
Hitomi Collaboration, 2016, Nature, 535, 117
Hopkins P. F. et al., 2018, MNRAS, 480, 800
Hopkins P. F., 2015, MNRAS, 450, 53
Huško F., Lacey C. G., 2022, MNRAS, 520, 5090
Huško F., Lacey C. G., Schaye J., Schaller M., Nobels F. S. J., 2022, MNRAS, 516, 3750
Iyer K. G. et al., 2020, MNRAS, 498, 430
Jacob S., Pfrommer C., 2017a, MNRAS, 467, 1449
Jacob S., Pfrommer C., 2017b, MNRAS, 467, 1478
Kaiser C. R., Alexander P., 1997, MNRAS, 286, 215
Kannan R., Vogelsberger M., Pfrommer C., Weinberger R., Springel V., Hernquist L., Puchwein E., Pakmor R., 2017, ApJ, 837, L18
King A., Pounds K., 2015, ARA&A, 53, 115
Komissarov S., Porth O., 2021, New Astron. Rev., 92, 101610
Laing R. A., Bridle A. H., 2014, MNRAS, 437, 3405
Lalakos A. et al., 2022, ApJ, 936, L5
Li Y. et al., 2020, ApJ, 889, L1
Li Y., Bryan G. L., 2014, ApJ, 789, 54
Li Y., Ruszkowski M., Bryan G. L., 2017, ApJ, 847, 106
Mandal A., Mukherjee D., Federrath C., Nesvadba N. P. H., Bicknell G. V., Wagner A. Y., Meenakshi M., 2021, MNRAS, 508, 4738
Mandelker N., Nagai D., Aung H., Dekel A., Padnos D., Birnboim Y., 2019, MNRAS, 484, 1100
Marinacci F. et al., 2018, MNRAS, 480, 5113
Martizzi D., Quataert E., Faucher-Giguère C.-A., Fielding D., 2019, MNRAS, 483, 2465
Massaglia S., Bodo G., Rossi P., Capetti A., Mignone A., 2022, A&A, 659, A139
McDonald M. et al., 2013, ApJ, 774, 23
McDonald M. et al., 2017, ApJ, 843, 28
McNamara B. R., Nulsen P. E. J., 2012, New J. Phys., 14, 055023
Meece G. R., Voit G. M., O'Shea B. W., 2017, ApJ, 841, 133
Mingo B. et al., 2019, MNRAS, 488, 2701
Mukherjee D., Bicknell G. V., Sutherland R., Wagner A., 2016, MNRAS, 461, 967
Mukherjee D., Bicknell G. V., Wagner A. Y., Sutherland R. S., Silk J., 2018, MNRAS, 479, 5544
Naab T., Ostriker J. P., 2017, ARA&A, 55, 59
Naiman J. P. et al., 2018, MNRAS, 477, 1206
Navarro J. F., Frenk C. S., White S. D. M., 1996, ApJ, 462, 563
Nelson D. et al., 2018, MNRAS, 475, 624
Ohlmann S. T., Röpke F. K., Pakmor R., Springel V., 2016, ApJ, 816, L9
Olivares V., Su Y., Nulsen P., Kraft R., Somboonpanyakul T., Andrade-Santos F., Jones C., Forman W., 2022, MNRAS, 516, L101
Omma H., Binney J., Bryan G., Slyz A., 2004, MNRAS, 348, 1105
Owen F. N., Ledlow M. J., 1997, ApJS, 108, 41
Padnos D., Mandelker N., Birnboim Y., Dekel A., Krumholz M. R., Steinberg E., 2018, MNRAS, 477, 3293
Pakmor R., Hachinger S., Röpke F. K., Hillebrandt W., 2011, A&A, 528, A117
Perucho M., Martí J.-M., Quilis V., 2019, MNRAS, 482, 3718
Perucho M., Martí J.-M., Quilis V., 2022, MNRAS, 510, 2084
Pillepich A. et al., 2018a, MNRAS, 473, 4077
Pillepich A. et al., 2018b, MNRAS, 475, 648
Prasad D., Sharma P., Babul A., 2015, ApJ, 811, 108
Prasad D., Voit G. M., O'Shea B. W., 2022, ApJ, 932, 18
Reynolds C. S., Balbus S. A., Schekochihin A. A., 2015, ApJ, 815, 41

Reynolds C. S., Heinz S., Begelman M. C., 2002, MNRAS, 332, 271

Ruszkowski M., Yang H. Y. K., Reynolds C. S., 2017, ApJ, 844, 13

Soker N., 2019, MNRAS, 482, 1883

Somerville R. S., Davé R., 2015, ARA&A, 53, 51

Springel V. et al., 2018, MNRAS, 475, 676

Springel V., 2010, MNRAS, 401, 791

Springel V., Hernquist L., 2003, MNRAS, 339, 289

Su K.-Y. et al., 2020, MNRAS, 491, 1190

Su K.-Y. et al., 2021, MNRAS, 507, 175

Su K.-Y., Bryan G. L., Haiman Z., Somerville R. S., Hayward C. C., Faucher-Giguère C.-A., 2023, MNRAS, 520, 4258

Tacchella S., Forbes J. C., Caplar N., 2020, MNRAS, 497, 698

Talbot R. Y., Bourne M. A., Sijacki D., 2021, MNRAS, 504, 3619

Talbot R. Y., Sijacki D., Bourne M. A., 2022, MNRAS, 514, 4535

Tanner R., Weaver K. A., 2022, AJ, 163, 134

Tillman M. T., Burkhart B., Tonnesen S., Bird S., Bryan G. L., Anglés-Alcázar D., Davé R., Genel S., 2022, ApJ, 945, L17

Torrey P. et al., 2020, MNRAS, 497, 5292

Vernaleo J. C., Reynolds C. S., 2006, ApJ, 645, 83

Vogelsberger M. et al., 2014a, MNRAS, 444, 1518

Vogelsberger M. et al., 2014b, Nature, 509, 177

Vogelsberger M., Genel S., Sijacki D., Torrey P., Springel V., Hernquist L., 2013, MNRAS, 436, 3031

Wang C., Ruszkowski M., Pfrommer C., Oh S. P., Yang H. Y. K., 2021, MNRAS, 504, 898

Weinberger R. et al., 2017a, MNRAS, 465, 3291

Weinberger R. et al., 2018, MNRAS, 479, 4056

Weinberger R., Ehlert K., Pfrommer C., Pakmor R., Springel V., 2017b, MNRAS, 470, 4530

Weinberger R., Hernquist L., 2023, MNRAS, 519, 3011

Wellons S. et al., 2023, MNRAS, 520, 5394

Yang H. Y. K., Reynolds C. S., 2016a, ApJ, 818, 181

Yang H. Y. K., Reynolds C. S., 2016b, ApJ, 829, 90

Yates P. M., Shabala S. S., Krause M. G. H., 2018, MNRAS, 480, 5286

Yates-Jones P. M., Shabala S. S., Power C., Krause M. G. H., Hardcastle M. J., Noh Velastín E. A. N. M., Stewart Georgia S. C., 2023, PASA, 40, 14

Zhuravleva I. et al., 2014, Nature, 515, 85

Figure A1. Same as Fig. 3, only with the slightly lower resolution simulation *rw jet a 4*.

APPENDIX A: JET PROPAGATION AT LOWER RESOLUTION

Fig. A1 shows the *rw jet a 4* simulation, which can be directly compared to Fig. 3. The most notable difference is the absence of KHI body modes in the momentum flux perpendicular to the jet propagation (bottom inlay). We speculate that the emergence of these internal effects causes the convergence in the jet position–time diagram (Fig. 4).
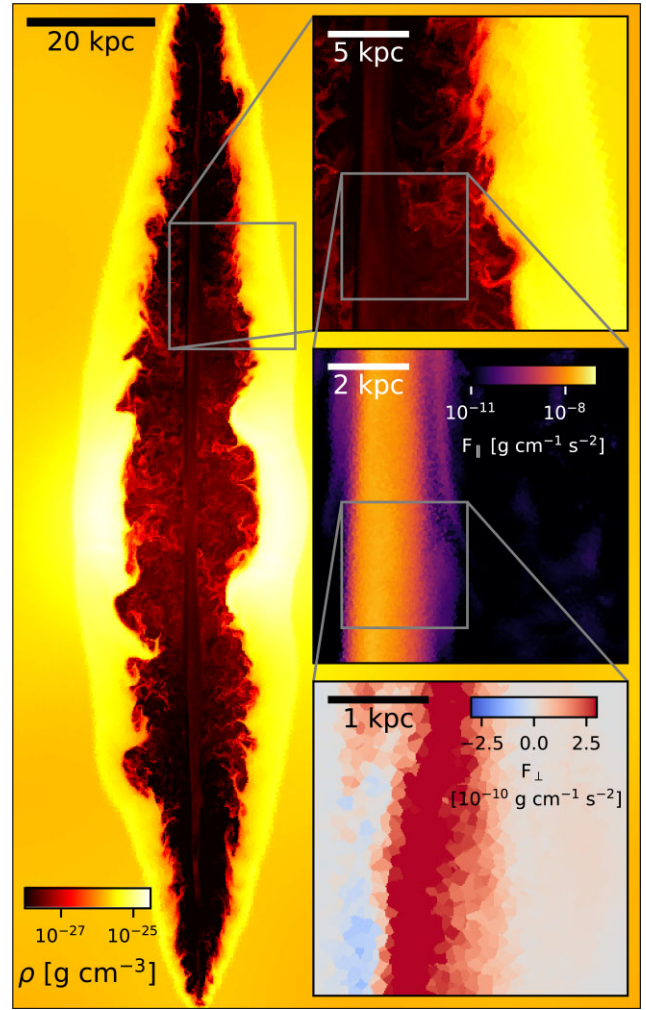
APPENDIX B: COOLING OVER FREE-FALL TIME VERSUS RADIUS FOR DIFFERENT CODES

Fig. B1 shows the cooling over free-fall time ratio for the respective simulations. Independent of which feedback model is employed, the outburst always causes significant amounts of gas with $t_c/t_{ff} < 10$ at radii larger than 30 kpc, with more efficient feedback leading to larger amounts of cooling gas at large radii.
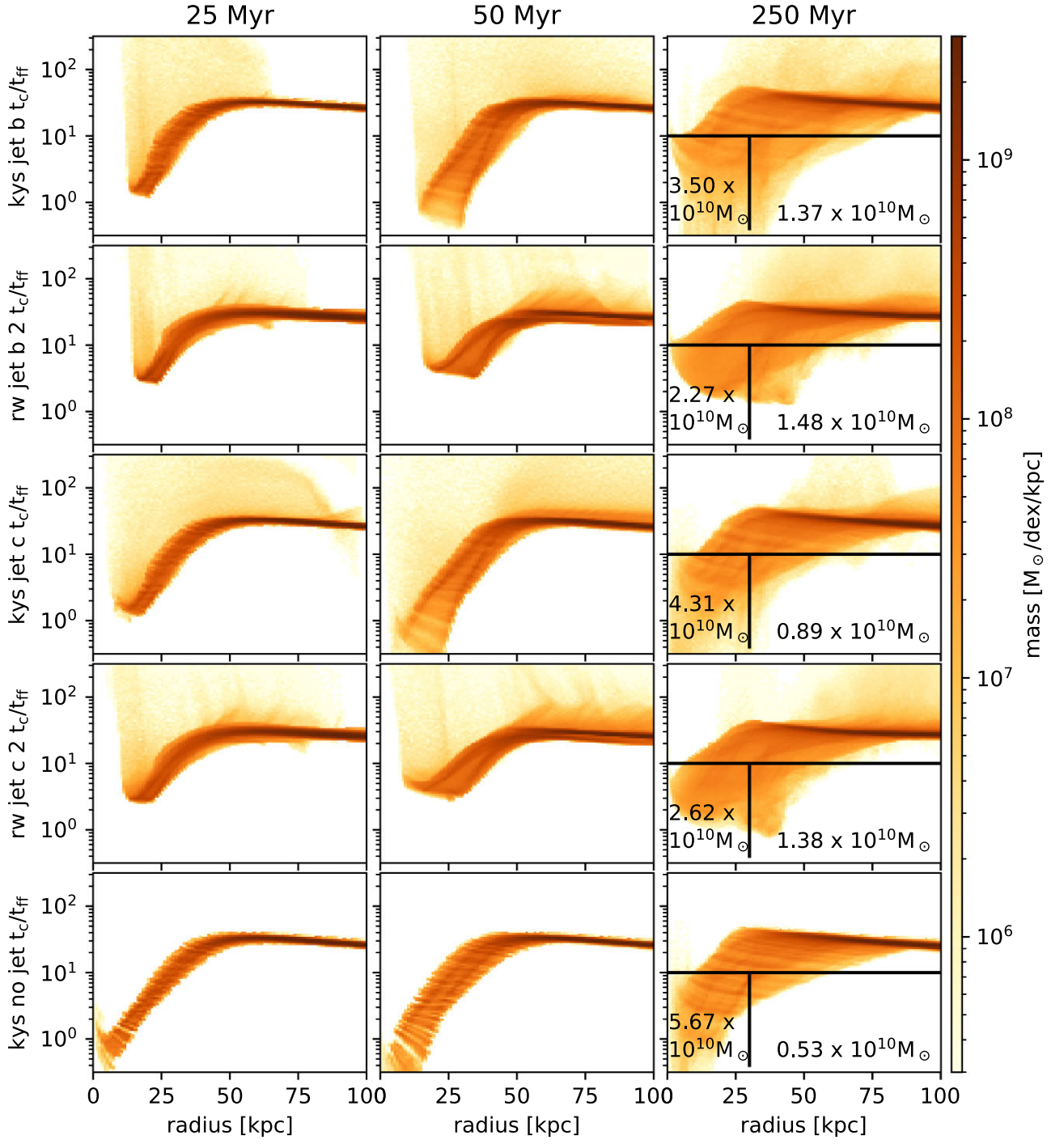
Figure B1. 2D histogram of cooling over free-fall time as a function of radius.

This paper has been typeset from a TeX/LaTeX file prepared by the author.